Plasma Sources
Science and
Technology

ACCEPTED MANUSCRIPT

Numerical study of surface charge dynamics and its feedback on the interaction between atmospheric pressure plasma jet and dielectric target

To cite this article before publication: Chenhua Ren *et al* 2025 *Plasma Sources Sci. Technol.* in press https://doi.org/10.1088/1361-6595/ae2266

Numerical study of surface charge dynamics and its feedback on the interaction between atmospheric pressure plasma jet and dielectric target

Chenhua Ren[1], Bangdou Huang[1,*], Cheng Zhang[1,2,*], Bo Qi[3], Weijiang Chen[4], Tao Shao[1,2]

1 Beijing International S&T Cooperation Base for Plasma Science and Energy Conversion, Institute of Electrical Engineering, Chinese Academy of Sciences, Beijing 100190, China

2 University of Chinese Academy of Sciences, Beijing 100049, China

3 North China Electric Power University, Beijing, 102206, China

4 State Grid Corporation of China, Beijing 100031, China

*Authors to whom correspondence should be addressed: Bangdou Huang, huangbangdou@mail.iee.ac.cn; Cheng Zhang, zhangcheng@mail.iee.ac.cn

Abstract

The surface charge dynamics due to the interaction between a nanosecond pulsed atmospheric pressure plasma jet (APPJ) and a grounded dielectric surface is investigated by two-dimensional axisymmetric fluid simulation. The development of APPJ can be divided into three stages: (1) the primary discharge, (2) the return and forward strokes, and (3) surface ionization wave (SIW). It is verified that the forward stroke plays a critical role on the polarity of surface charges, which can be further controlled by pulse parameters (*e.g.* pulse width and voltage amplitude). The enhanced forward stroke, characterized by an elevated electric field with a relatively uniform distribution along the APPJ channel, raises the potential drop across the plasma column and creates the conditions for the field reversal near the target. These flip the axial electric field and drive electrons moving towards the target, as a result of which, the polarity of surface charges reverses. This indicate that as the potential drop cross the plasma column exceed the applied voltage, the direction of electric field revers and can cause the polarity reversion of surface charge. Thus, the reversal instant can happen at the voltage plateau, the voltage falling edge or after the applied voltage has reduced to zero. Due to the time sequence of surface charge reversing at different radial positions, which induces a remarkable radial field component, a negative SIW further develops along the dielectric target. As feedback, this phenomenon results in both enhanced net charge transfer to the dielectric and intensive energy deposition (electron Joule heating) of APPJ in the vicinity of the target. This study opens a new route towards the application optimization of APPJ in multiple fields via the feedback effect of surface charges on APPJ-surface interaction.

Keywords: nanosecond pulsed discharge, atmospheric pressure plasma jet, surface charge, return stroke

1. Introduction

Atmospheric pressure plasma jet (APPJ) driven by nanosecond voltage pulses is characterized by its unique non-equilibrium feature (*e.g.* low temperature and abundant active species) under transient high power density [1-4]. As one of the promising discharge formats, APPJ can deliver high electric field, radiation, as well as a wide range of active and charged species for remote localized treatment [5,6], showing great potential in various fields, such as bio-medicine [7,8], agriculture [9], and material modifications [10,11].

Interactions between the plasma and the surface are critical in practical applications [6,12]. The impingement of discharge and the evolution of the electric field directly affect the fluxes of active and charged species to the surface, which further influences its electrical and chemical properties [13-15]. In turn, the permittivity, conductivity, and morphology of the surface greatly alter the discharge dynamics [16-20], *e.g.* the appearance of the return stroke and the surface ionization wave (SIW). Revealing the fundamental process of plasma-surface interaction is essential for the optimization of plasma devices.

Dynamics of surface charging (accumulation and dissipation) is one of the decisive processes on the discharge kinetics and the energy deposition (electron Joule heating) among the interactions [21,22], whose properties have been explored both experimentally and numerically. The accumulation of surface charges is demonstrated by a significant electric field offset before the discharge pulse with the electric field-induced second harmonic (E-FISH) method [23,24]. Besides, it is impressive that the quantification of leftover charges is realized by assessing the electric field inside a dielectric material, based on the combination of the Pockels technique and the simulations [25-29].

Generally, since the charging is caused by the impact of the discharge, surface charges deposited on the dielectric has the same polarity with that of the applied voltage [30-33]. However, charges having opposite polarity can be observed shortly after the fall of the pulse in some cases [33,34]. The reversal of surface charge polarity is closely related to the ignition of secondary streamers, which can be identified by current signals as reported in reference [35]. For example, with the excitation of sinusoidal voltage waveform, a weak charged region is observed at the center part of the positive

discharge after the applied voltage drops to zero, due to the occurrence of secondary discharge between the powered electrode and the residual surface charge [34]. With a positive pulse train, a reversed field offset induced by surface charges near the powered electrode appears before the next discharge pulse, while it has the same sign as the pulse at the positions farther away [23,36]. This phenomenon is usually attributed to the opposite electric field (reverse potential gradient) generated between the plasma channel and the contact surface, leading to electron absorption or ion neutralization near the target [25,35,37].

It should be noted that, after the discharge impacts the grounded dielectric target, besides the SIW along the surface, there are two strokes in space, which first propagates from the target to the powered electrode (return stroke) and then reverses its direction and further develops to target again (forward stroke) [30,38,39]. The return stroke propagates in extremely high speed (~10^6 m/s) [40] while with a weakened electric field, which causes that the secondary peak of electric field can only be captured near the target [41]. In contrast, the forward stroke greatly enhances the electric field in the channel and appears a relative uniform distribution [42,43]. These suggest that both the two strokes can cause the redistribution of electric field in the discharge channel, which may promote the recombination between charges or the ionization process [6]. The simulation results [40] also show that, after the multiple strokes, the flux of active species reaching the dielectric surface significantly increases, which indicates that the stroke process may also affect the accumulation of surface charge.

Since the surface charges accumulated on the target essentially determine the discharge dynamics, the uncertainties of the deposited amount and polarity complicate the plasma-surface interaction. The relationship among the discharge properties, surface charge dynamics, and its feedback effect on the energy deposition is still far less well known. Thus, studies on this fundamental process are required to advance the understanding of APPJ-surface interaction.

In this work, the interaction between the APPJ and the grounded dielectric target is investigated by using a two-dimensional (2D) axisymmetric fluid model. The impact of pulse parameters on the discharge evolution and the correlation between the properties of return and forward strokes and the surface charge dynamics are obtained. The feedback effect of surface charges on the discharge kinetics and energy deposition is illustrated.

2. Model description

The numerical model of the Ar/air plasma jet is conducted based on the 2D PASSKEy (PArallel Streamer Solver with KinEtics) framework [44], by solving the drift-diffusion-reaction equations for charged and neutral species, the electron energy conservation equation, and the Poisson equation (both volume and surface charge) for the electric potential. Detailed methods and benchmarks for the fluid model can be referred to [45]. The photoionization model for Ar/air mixture are developed and implemented in this work. Details on the methods can be found in the Appendix.

The 2D axisymmetric computational domain 10 × 12 mm is shown in figure 1(a). To avoid influencing the results [46], the Neumann boundary condition is applied to the radial boundary r = 10 mm. The Poisson equation is solved in the entire domain, while the continuity equations for species are only solved in the plasma region to reduce the computational burden. An annular powered electrode (red region) with a thickness of 50 μm and a length of 2 mm is set inside the dielectric tube. The dielectric tube, with a relative permittivity of ε_r = 4, a length of 4 mm, an inner radius of 0.75 mm, and an outer radius of 1.5 mm, is used. The dielectric target plate, with a relative permittivity of ε_r = 4 and a thickness of 150 μm, is attached to the ground. The distance between the tube outlet and the target is 8 mm. These parameters are selected refer to our previous work [47], *i.e.* the inner and outer diameter of quartz tube are the same. However, in order to save the computational resource, we reduce the distance from the tube outlet to the grounded dielectric target. The mesh size is set as 2 μm at the gas-target interface and 5 μm at the rest of computational domain. The mesh size selected is refine enough to capture the floating feature of the positive SIW above the dielectric surface, which has been tested in our previous work [36] and reference [48]. There are 552×2469 cells in the computational domain. For a complete simulation, the typical computational time is ~9 days.

Through the dielectric tube, the gas mixtures Ar/O_2 = 99/1 with a flow rate of 0.5 L/min is injected into the ambient air (N_2/O_2 = 80/20). Since the duration of the voltage pulse applied in this work (50 ns, as shown below) is far less than the time scale making the gas heating effect significant (on the order of microseconds [49]), the gas temperature is set at 300 K in the APPJ simulation [26,40]. The steady flow field of the neutral components (figure 1) is obtained by solving the compressible Navier-Stokes equations without the discharge, which is conducted based on the COMSOL software [50].

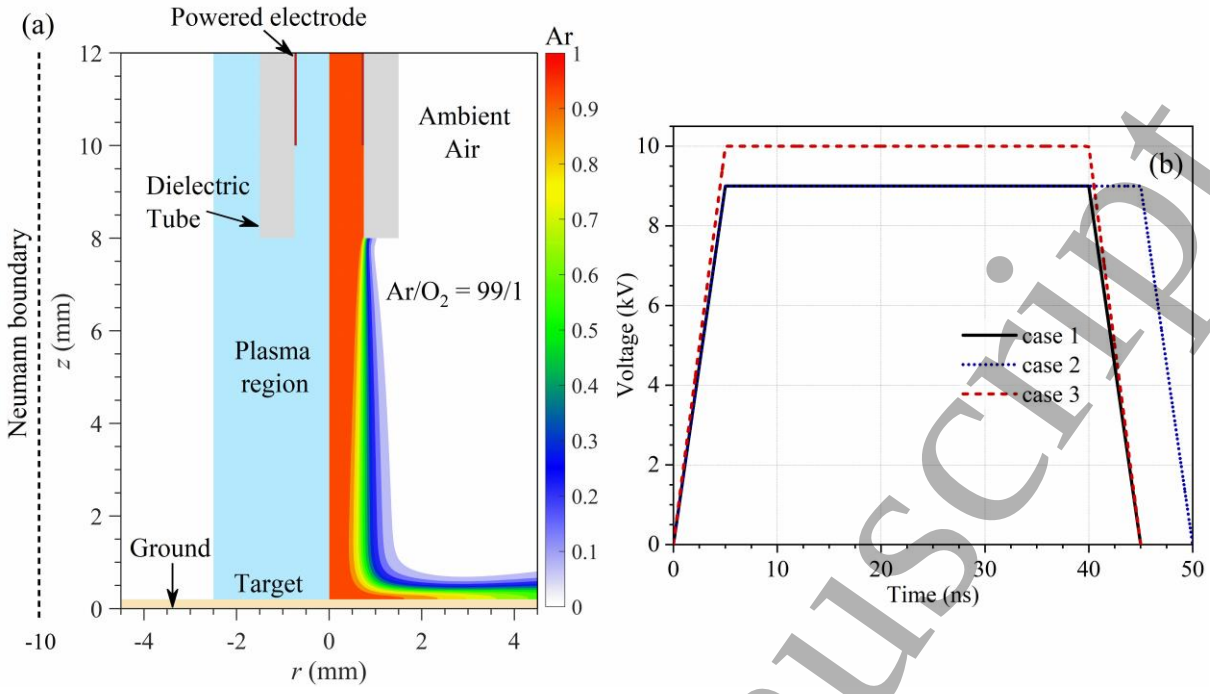

Figure 1. (a) Geometry of the computational domain (left) and Ar flow field without discharge (right), and (b) waveforms of voltage pulses applied to the powered electrode.

The chemical scheme for $Ar/N_2/O_2$ contains 20 species and 104 reactions. The following species are included in the model: e, Ar^+, Ar_2^+, N_2^+, O_2^+, N_4^+, O_4^+, $O_2^+N_2$, O_2^-, O^-, $Ar(1s_5)$, $Ar(1s_2)$, $Ar(2p_1)$, Ar_2*, $N_2(A^3\Sigma_u^+)$, $N_2(B^3\Pi_g)$, $N_2(C^3\Pi_u)$, N, O, and $O(^1D)$. The reaction mechanism for $Ar/N_2/O_2$ refers to [51-54] and is listed in the appendix. The transport parameters and rate coefficients are calculated by the Boltzmann solver Bolsig+ [55] based on the cross sections taken from the LXCat database [56], and tabulated as functions of both the fraction of gas mixture and the local mean electron energy. The initial charge density is set as 10^{10} m^{-3} and is uniformly distributed based on quasi-neutrality. The secondary electron emission coefficient γ by ion impact on the surface is taken as 0.1. The rather high value of secondary electron emission coefficient ($\gamma = 0.1$) selected in this work is in order to roughly consider other secondary emission processes, such as photoemission and secondary emission by the impact of metastable species [6,27].

The voltage waveforms applied on the powered electrode are given in figure 1(b), aiming to demonstrate the interaction between the plasma and the dielectric surface. For the basic condition (case 1), the voltage parameters are set as: the rising and falling edge are 5 ns, and the pulse width W_p is 35 ns with the amplitude V_a of 9 kV. It has been already known that changing the pulse width or the voltage amplitude can significantly affect the accumulation of surface charges by altering the

charging time (from the moment impact till the voltage pulse end) [25,26,57]. Based on this, the other two operating conditions are obtained by extending W_p to 40 ns (case 2), and by elevating V_a to 10 kV (case 3), respectively.

3. Results and discussion

3.1 Streamer dynamics of APPJ

The typical structure and evolution of the positive APPJ are first given. The temporal-spatial distribution of the electron density n_e, the electron impact ionization source S_e, the electric field E, and the potential Φ under the voltage pulse for case 1 are presented in figures 2 and 3. S_e is the net source term of electrons including the direct impact ionization and the stepwise ionization processes, which can be used to characterize the discharge kinetics.

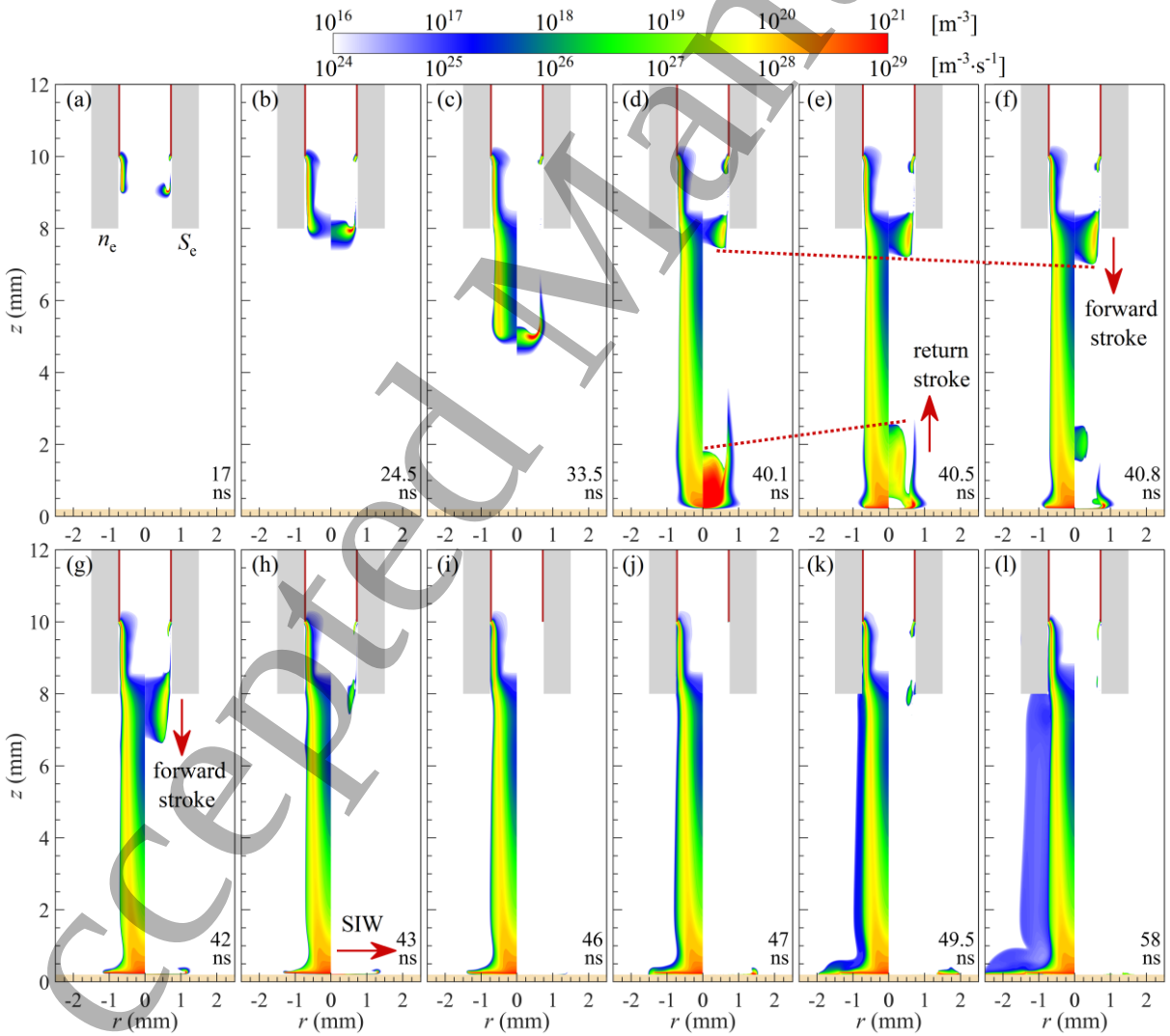

Figure 2. Evolution of electron density n_e (left part) and electron source S_e (right part) before and after the APPJ interacts with the target. Conditions: case 1, V_a = 9 kV and W_p = 35 ns.

The discharge is initiated at the tip of the powered electrode and then propagates along the inner surface of the tube as a positive SIW (17 ns), which is floating above the surface, and an ion-rich (or sheath-like) region is formed between the plasma channel and the dielectric tube [36,48]. As approaching the tube outlet (24.5 ns), the coverage of S_e increases, leading to the deflection of the SIW front towards the axis.

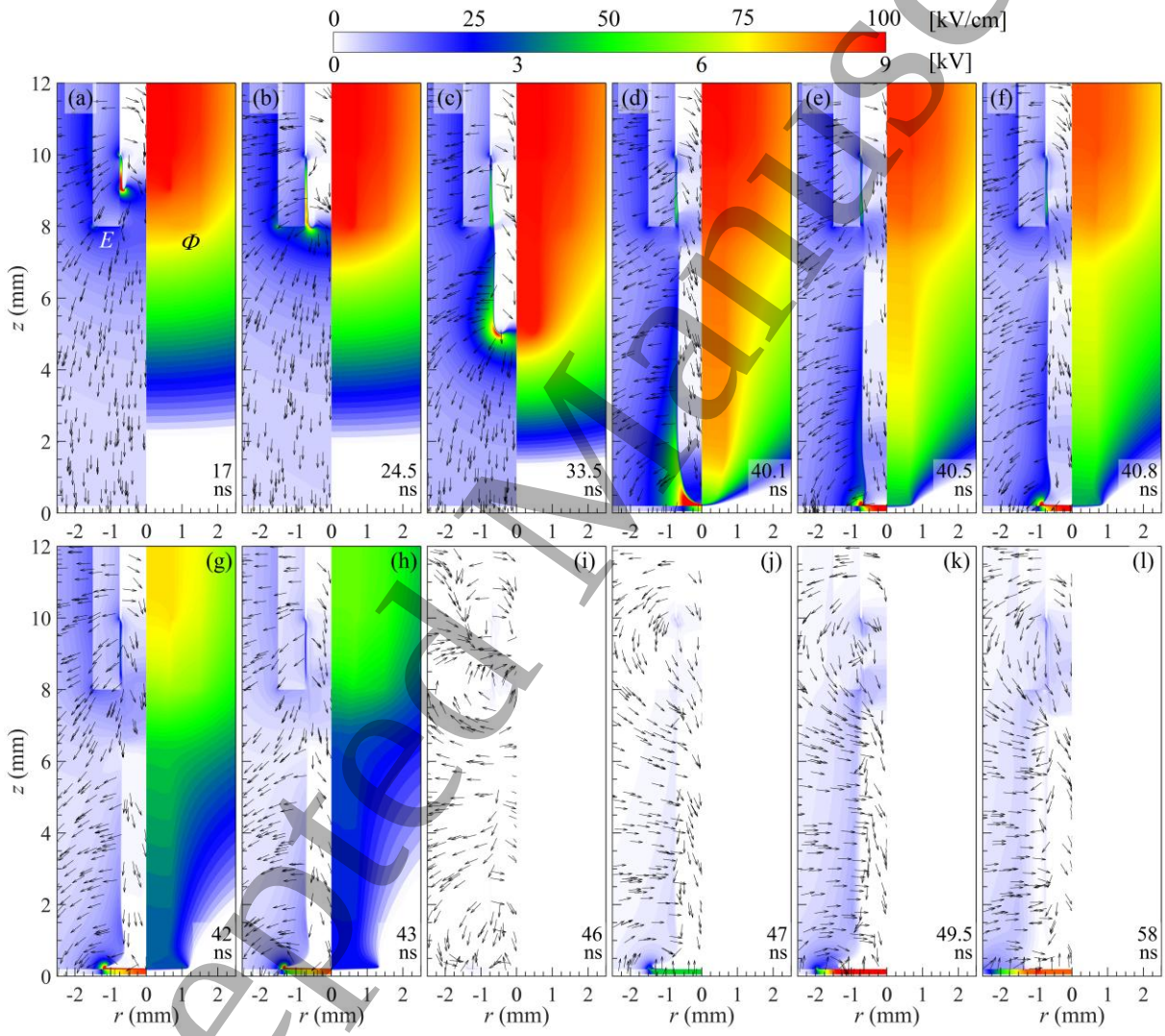

Figure 3. Evolution of electric field E (left part) and potential Φ (right part) before and after the APPJ interacts with the target. Conditions: case 1, V_a = 9 kV and W_p = 35 ns.

Then, the discharge moves from being attached to the inner surface of the tube into the space, and further guided by the mixed layer of Ar/air. S_e is mainly concentrated at the front of the ionization

wave, and gradually shrinks to the axis (24.5-40.1 ns), forming a solid contact point when it reaches the target (primary discharge). At this instant, a return stroke appears and propagates towards the powered electrode at an extremely high speed ~4.1×10^6 m/s (40.1-40.8 ns). After that, a forward stroke (40.8 ns) develops originating from the tube outlet and the powered electrode, and S_e keeps a continuous profile along the APPJ channel.

After contacting the surface, a positive SIW is formed and further propagates on the target in the radial direction. n_e in the SIW channel is further elevated compared to the primary stage. During the voltage falling edge, both the forward stroke in space and the SIW on target stop propagating and decay slowly versus time (42-43 ns).

The field reverse occurs after the end of the voltage pulse (46 ns), at which instant both the electric field and the potential are too weak to obverse. In addition, there is no obvious production of electrons near the target at the reversing instant of electric field. Subsequently, the electric field near the target raises again (49.5 ns), indicating that the polarity of surface charge has reversed. The surface discharge continuously develops and can directly contact the dielectric target, transforming from a positive into a negative SIW. Finally, the discharge intensity gradually declines.

The above obtained development of APPJ can be divided into three stages: primary discharge (including the SIW within the tube and the forward IW in space, with time interval of 0~40.1 ns), return and forward strokes (including a return propagating to the powered electrode and then a forward propagating to the target again, with time interval of 40.1~43 ns), and the SIW along the target (with time interval of 43~58 ns). These findings correlate with the previous results [25,40].

The discharge dynamics (n_e and S_e) of cases 2 and 3 are also presented, as shown in figures 4 and 5. It is found that by extending the pulse width or elevating the voltage amplitude, the length of the forward stroke increases significantly, which prolongs from ~1.2 mm in case 1 to ~4 mm in case 2 and ~7.4 mm in case 3. In addition, the direction reverse of the electric field near the dielectric target occurs at 47 ns and 36.8 ns, which locates at the falling edge and the plateau, respectively. After that, the SIW on the target also transforms from the positive into the negative polarity and further develops in radial direction. Subsequently, with the reduction of voltage, n_e in the channel gradually diffuses towards the volume and S_e gradually decays.

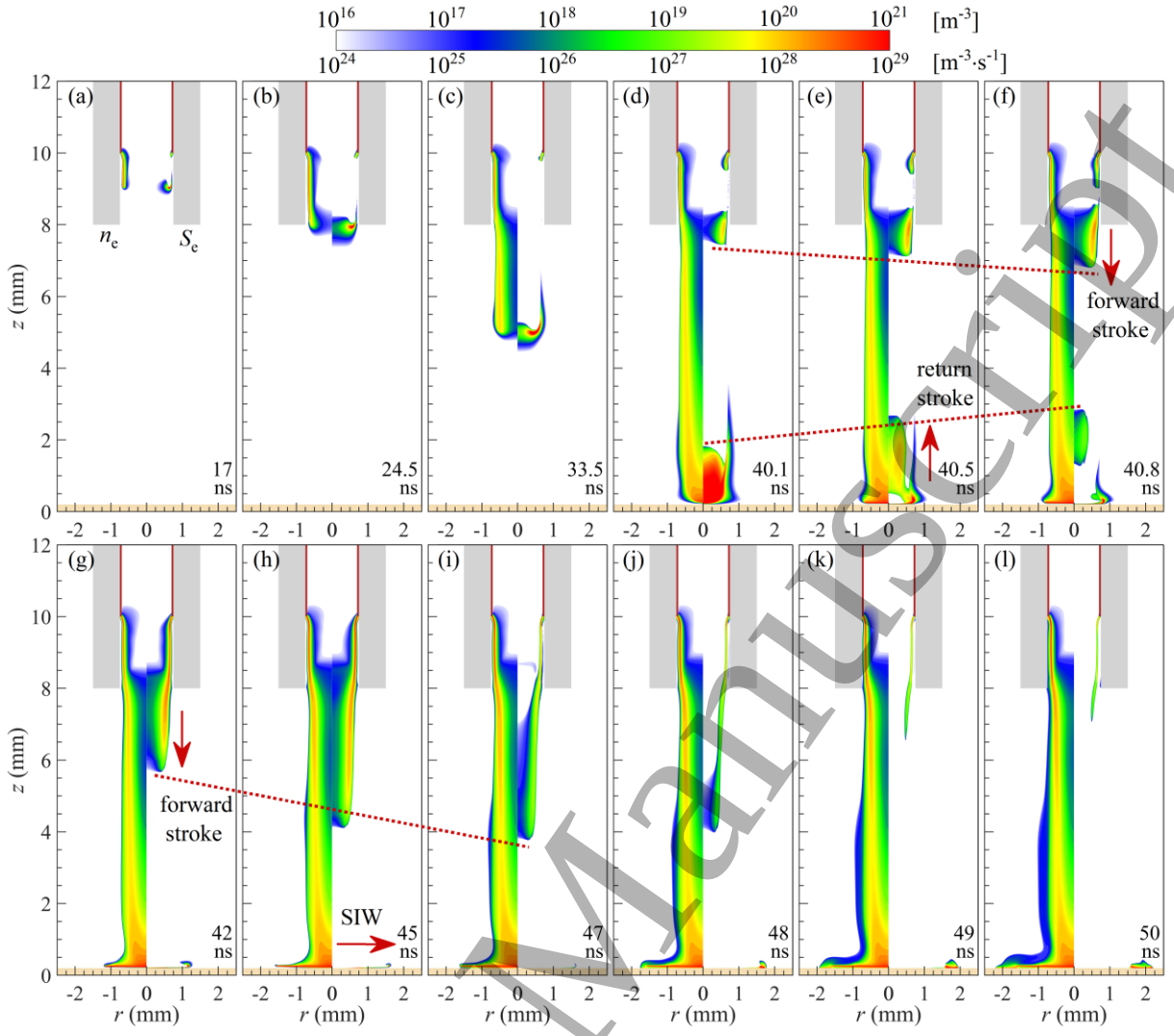

Figure 4. Evolution of electron density n_e (left part) and electron source S_e (right part) before and after the APPJ interacts with the target. Conditions: case 2, V_a = 9 kV and W_p = 40 ns.

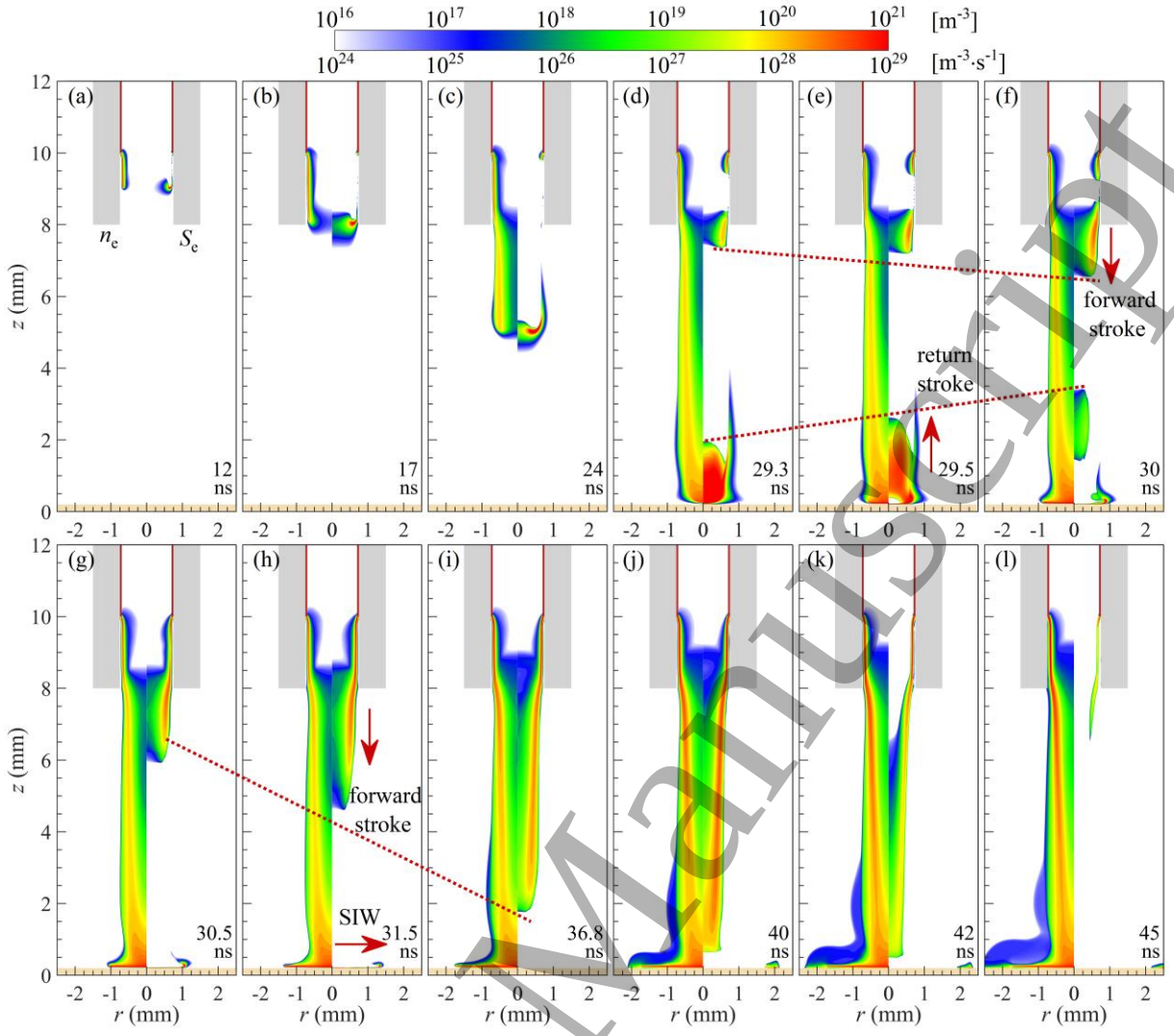

Figure 5. Evolution of electron density n_e (left part) and electron source S_e (right part) before and after the APPJ interacts with the target. Conditions: case 3, V_a = 10 kV and W_p = 35 ns.

3.2 Surface charge dynamics on the target

Figure 6 presents the spatial and temporal evolution of the surface charges on the grounded target for different voltage pulses. In order to clearly show the weak distribution of surface charge, σ is shown in the log scale. With the basic condition (case 1), the surface charge increases abruptly after the primary discharge impact on the target, and its quantity decreases as the distance away from the axis (r = 0 mm) increases, which indicates the trajectory of the SIW along the target. At the pulse end, the polarity of the surface charge σ remains positive and is consistent with that of the applied voltage. However, by extending the calculation time after the voltage pulse end, the polarity of surface charge reverses at ~46.1 ns.

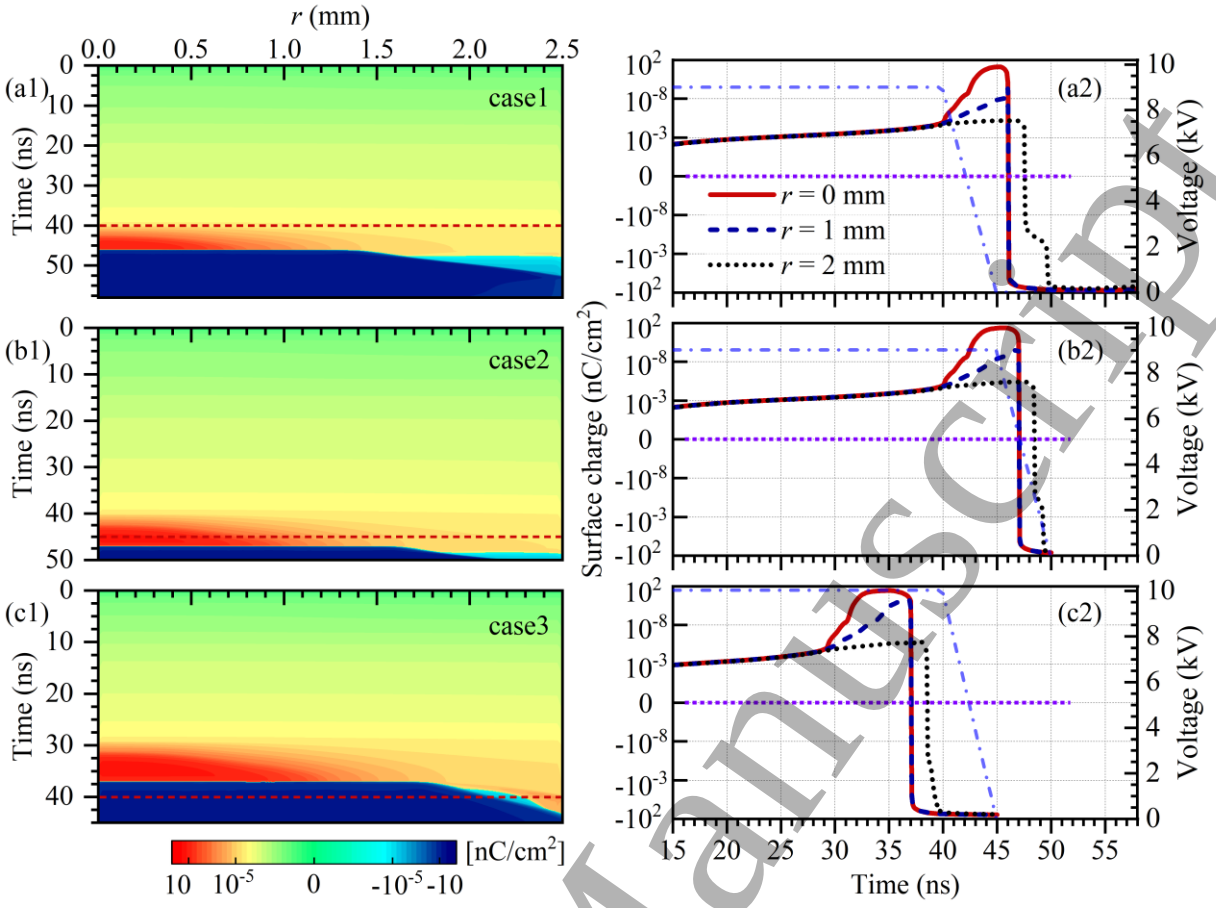

Figure 6. Spatial and temporal evolution of the surface charge σ on the grounded target with different voltage pulses (left column a1, b1 and c1, red dashed lines indicate the start of voltage falling edge), and dynamics of σ at different locations along the path of SIW (right column a2, b2 and c2).

By extending the pulse width (case 2) or elevating the voltage amplitude (case 3), it is found that the polarity of the deposited surface charge transforms from positive to negative under both conditions. The reversal instants appear at the falling edge and the plateau of the voltage pulse, respectively. σ at the central region (r < 1 mm) has a larger magnitude compared to the target periphery (r = 2 mm) both before and after the polarity reverse, and there is a time lag on the charge reversal along the radial positions.

Typically, the surface charge density in references [30,58] ranges from 0.1~1 nC/cm^2, which is less than the maximal surface charge density obtained in this work ~40 nC/cm^2. However, the operating condition is significantly different in three aspects, *i.e.*, voltage peak, target thickness, and tube outlet-target distance. In references [30,58], besides a lower voltage peak and a thicker dielectric

target is applied, the distance between the tube outlet and the dielectric target (3 cm) is far larger than the operating conditions in this work. As reported in reference [35], an increased distance from the APPJ tube outlet to the dielectric surface results in a decreased charge deposition. Thus, these cause a weakened discharge as contacting the target and less surface charge accumulation along the dielectric surface.

To reveal the complex dynamics of surface charging, the 2D spatial distribution of n_e and E near the target, the evolution of the axial component of the electric field E_z above the target (with a distance of 1 μm), and the electron flux $\boldsymbol{\Gamma}_e$ towards the target are given in figures 7-9 for different voltage pulses (case 1-3), respectively. The contours are plotted in log scale (10^{16}~10^{21} m^{-3}) for n_e, and in linear scale (0~200 kV/cm) for E. E_z is positive as pointing upward. $\boldsymbol{\Gamma}_e$ is positive as propagating away the target. It is first positive and the dashed lines with arrow indicate the instant of polarity reverse for $\boldsymbol{\Gamma}_e$.

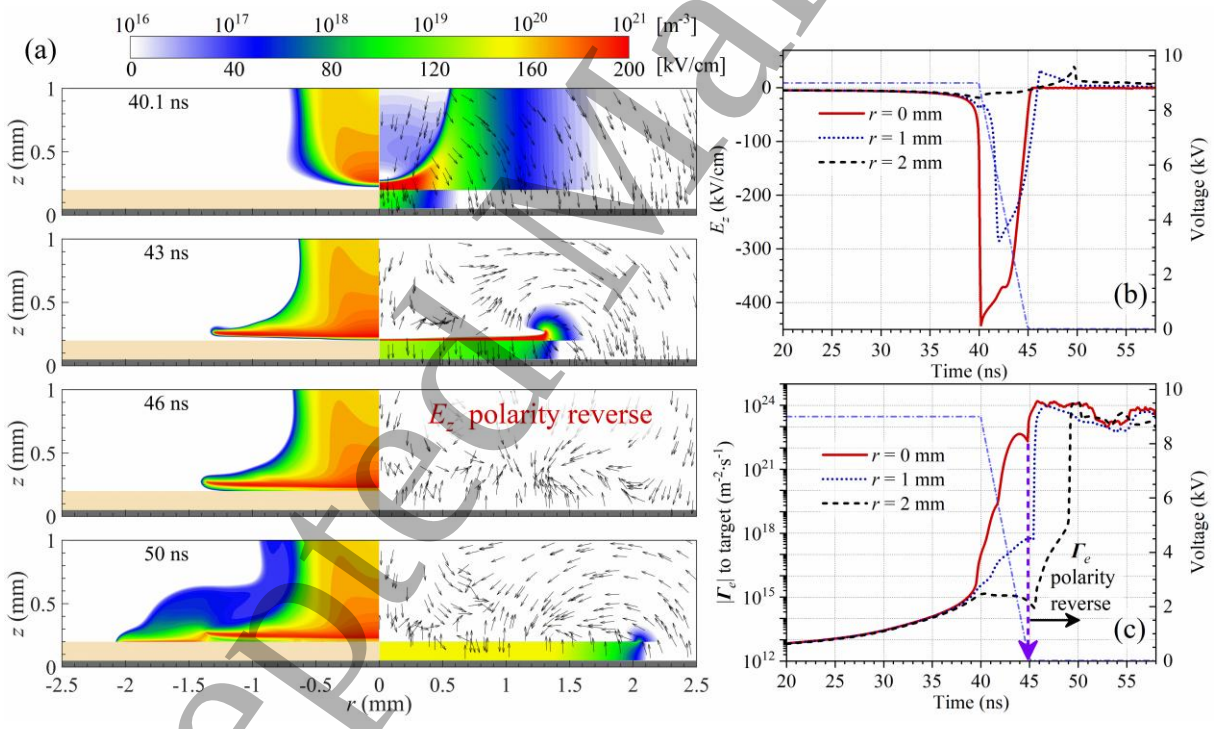

Figure 7. (a) Spatial distribution of electron density n_e (left part) and electric field E (right part) near the target, (b) evolution of the axial component of electric field E_z above the target, and (c) $|\boldsymbol{\Gamma}_e|$ to target. Conditions: case 1, V_a = 9 kV and W_p = 35 ns.

As for the basic condition (case 1), the induced SIW along the target shows the typical features

of the positive surface discharge, that an ion-rich gap with a thickness of ~10 μm and characterized by the large electric field is formed (figure 7(a)). During the voltage falling edge, the drop of E_z intensity weakens the proportion of the drift term along the field direction, especially in the central region (figure 7(b)).

Meanwhile, the electron flux propagating away from the target surface first increases due to the approaching of the positive streamer, and then gradually reduces until its direction reverses. This means that the diffusion towards the target becomes dominant for electrons in the discharge channel under the weakened electric field, neutralizing the strong electric field in the sheath-like region. This makes that before the electric field above the dielectric target is completely reversed, the amount of surface charge accumulated has begun to decline slowly. This explains the increment of n_e near the target and the reduction of σ at r = 0 mm at the falling edge (figure 6(a2)). Besides, although E_z reverses its direction to a weak value near the pulse end, the polarity of σ remains consistent with the voltage pulse (figure 6(a1)). Further extending the calculation time, the polarity of σ reverses.

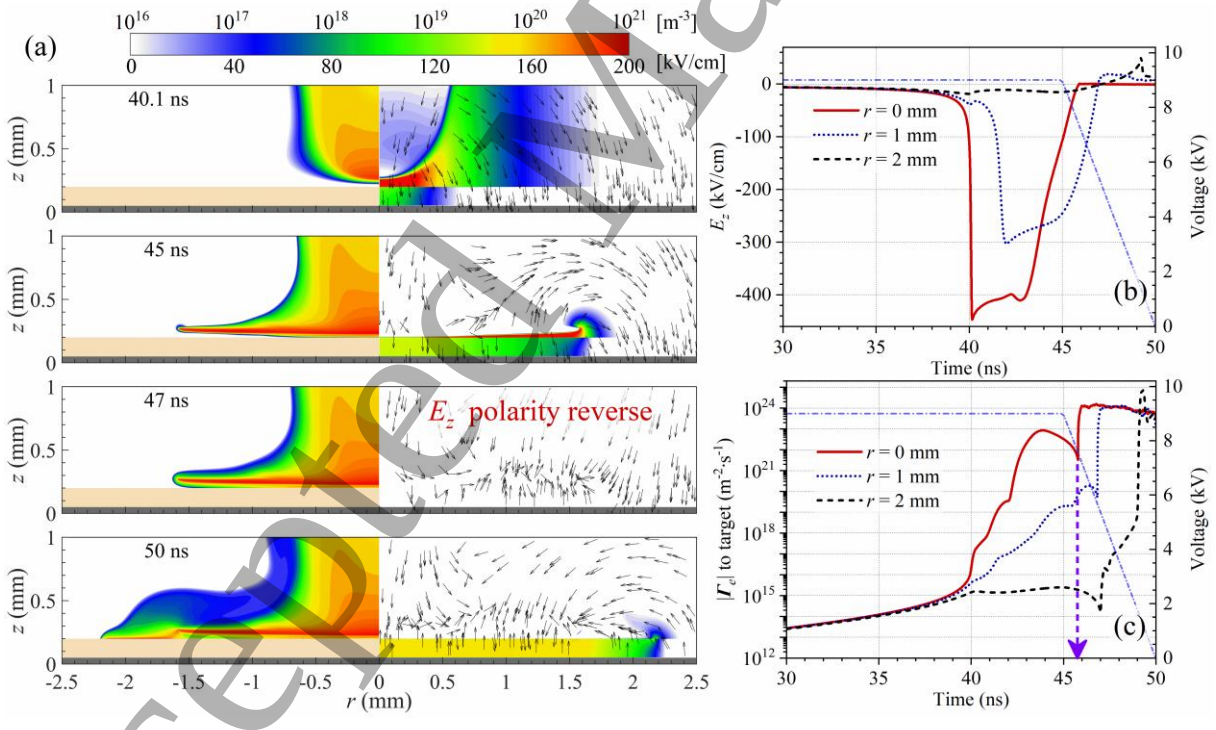

Figure 8. (a) Spatial distribution of electron density n_e (left part) and electric field E (right part) near the target, (b) evolution of the axial component of electric field E_z above the target, and (c) $|\boldsymbol{\Gamma}_e|$ to target. Conditions: case 2, V_a = 9 kV and W_p = 40 ns.

Figure 8 shows the effect of the extended pulse width on the discharge properties near the target. At the start of the voltage falling edge (45 ns), E_z drops to almost zero, and the formed sheath-like region with the intensive electric field disappears, leading to the direct contact of the SIW channel with the target within the central region. The amplitude of E_z first reduces to zero and then increases in the opposite direction (figure 8(b)), which drives electrons moving towards the target and then leads to the σ polarity reverse. Similar findings can be observed in several dielectric barrier discharge (DBD) structures, which usually contribute to the backward breakdown between the plasma channel and the dielectric/electrode when the applied voltage drops or changes polarity [23,33-36].

In addition, by increasing the voltage amplitude (case 3), the phenomenon of the σ polarity reverse is also observed (figure 6(c)). As shown in figure 9, the electron flux towards the target significantly increased after the instant of E_z reversal. Note that, in this case, the σ polarity reversal occurs at the voltage plateau, which indicates that the reversal of the electric field is independent of the role of the voltage falling edge.

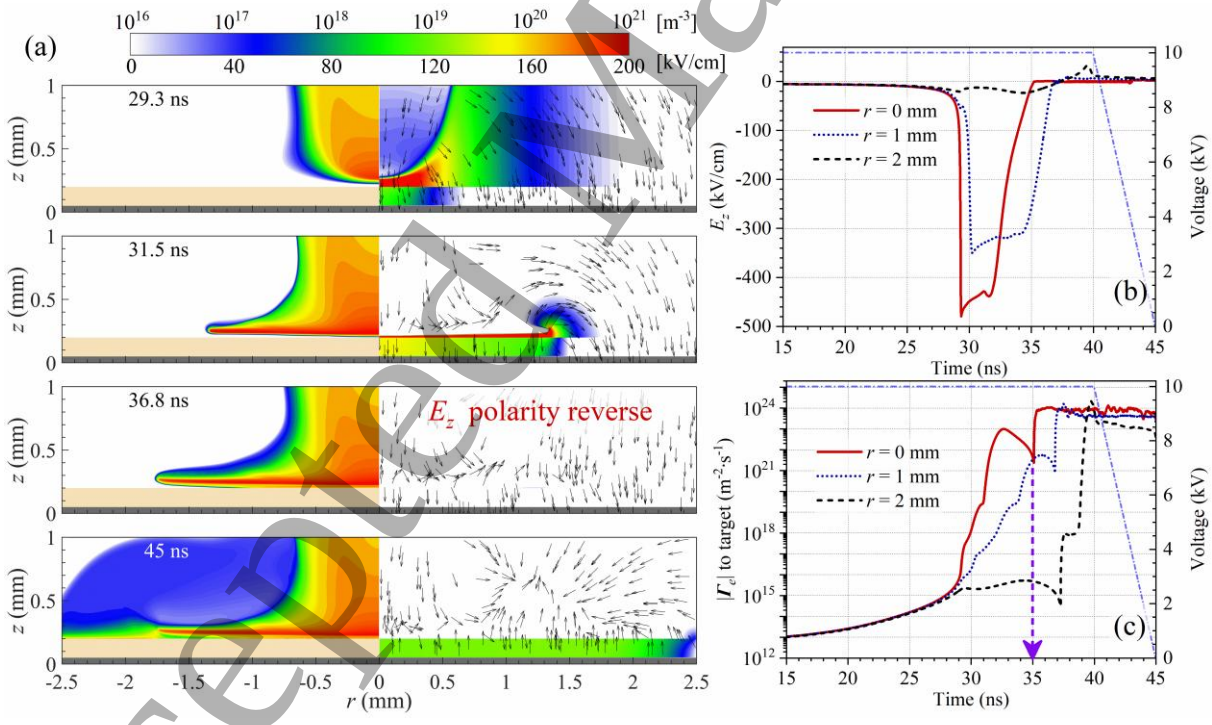

Figure 9. (a) Spatial distribution of electron density n_e (left part) and electric field E (right part) near the target, (b) evolution of the axial component of electric field E_z above the target, and (c) $|\boldsymbol{\Gamma}_e|$ to target. Conditions: case 3, V_a = 10 kV and W_p = 35 ns.

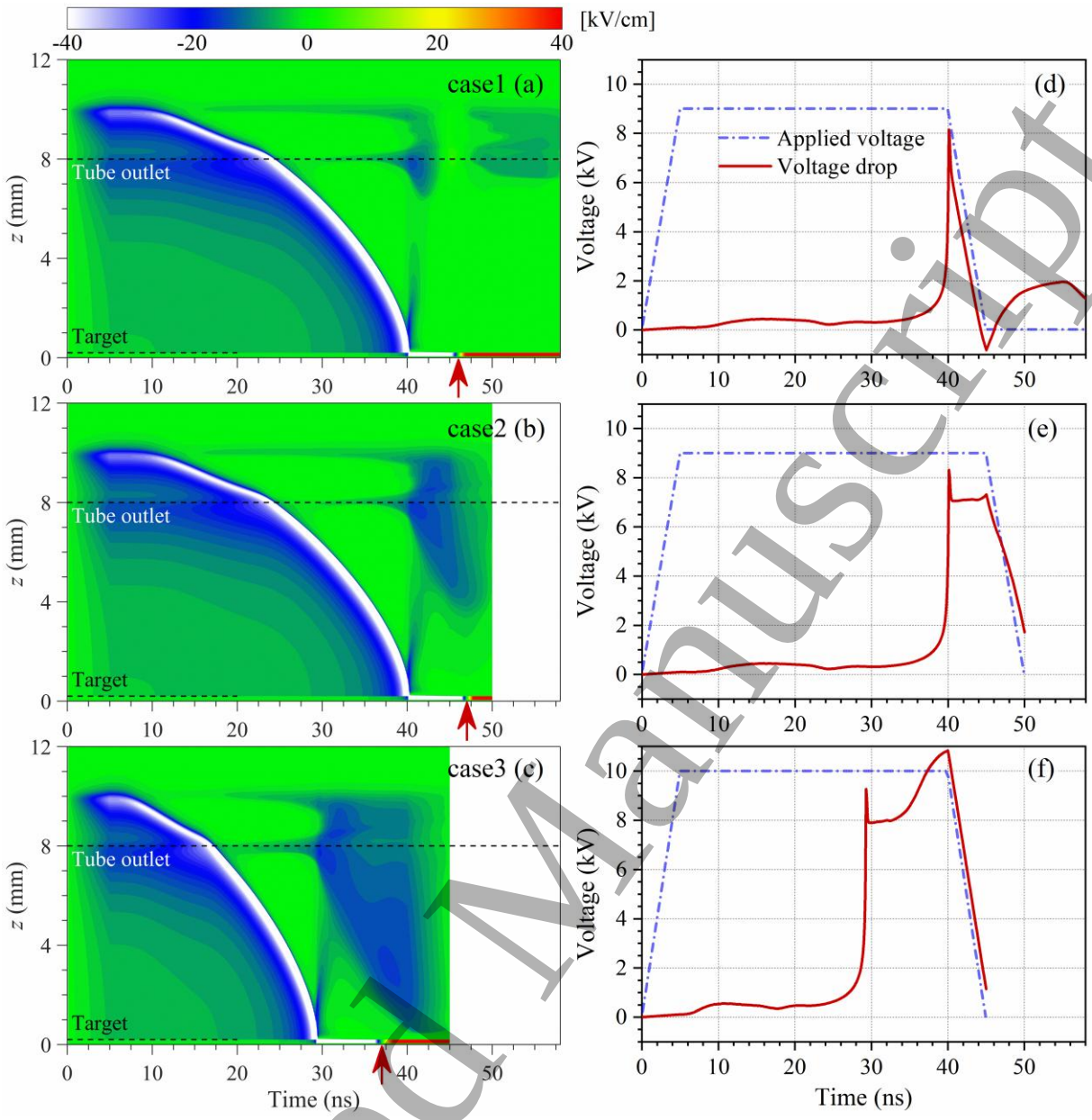

Figure 10. (a-c) Spatial and temporal evolution of the axial component of electric field E_z, and (e-f) the potential drop across the plasma column from the powered electrode along the axial line $r = 0.5$ mm for different voltage pulses case 1-3. Dashed lines indicate the position of tube outlet and target, and red arrows are the instant of E_z reverse.

It should be noted that due to the limited spatial resolution of the ICCD camera, it is still challenge to direct observe the phenomenon that the positive SIW floats above the surface or the negative SIW sticks to the surface. the experimental observations [59] show that the positive streamer branches as approaching the dielectric and all of these channels bent towards the surface, which indirectly indicates that the gas-phase primary streamer does not reach the dielectric. In addition, the

behavior of positive and negative SIW have been explored by fluid and PIC/MCC simulations [48,60,61].

Figure 10 presents the temporal evolution of the electric field magnitude E at the axial line r = 0.5 mm. The potential drop across the plasma column is obtained by integrating E_z from the powered electrode to the upper surface of the grounded dielectric target along the axial line r = 0.5 mm, while the potential drop across the dielectric is not included. During the development of the primary discharge, the maximum of E only appears at the front of the IW and gradually increases as it approaches the target. After that, the APPJ operates in the return and forward strokes stage, with the properties that E is almost uniformly distributed along the APPJ channel, and its intensity is significantly elevated from ~0.4 kV/cm to ~10-13 kV/cm. These features qualitatively correlate with the previous simulations and experiments [43,62].

As the discharge impacts the target, positive charges are first deposited on the dielectric surface (figure 6). Considering the opposite direction between the electric field at the front of IW and that induced by the positive σ, there is a competition for obtaining the charged species within the sheath-like region. As shown in figure 10(b-c), both the extension of the pulse width and the increment in the voltage amplitude promote the development of the forward stroke, resulting in a sharp increment of the potential drop along the APPJ channel from the powered electrode to the front of IW (figure 10(e-f)). Consequently, the potential at the discharge front is remarkably reduced, changing E_z to the opposite direction and promoting the motion of electrons towards the target. As indicated by the arrows, there is the weakest E near the surface before the instant of the σ polarity reverse. As the potential drop cross the plasma column exceeds the applied voltage, the direction of electric field reverses, which can further lead to the polarity reversal of surface charge. The reversal instant can happen at the voltage plateau, the voltage falling edge or after the applied voltage has reduced to zero, which depends on the competitive relation between the potential drop and the applied voltage. Similar phenomenon is reported in references [23,26,33-36].

The above results show that the intensity of the forward stroke can be adjusted by varying the pulse parameters, such as pulse width and voltage amplitude, which further affects the direction of E_z near the target and the surface charge dynamics. Extending the pulse width or elevating the voltage amplitude essentially increases the charging time [25,26,57], both of which present the similar effect

on the surface charge. As demonstrated in reference [57], a longer pulse width can directly control the amount of changing during the voltage pulse, and a larger voltage amplitude can significantly alter the propagation velocity of IW and thus changes the impact instant, resulting in a longer changing time till the end of the pulse. This suggests that the plasma-surface interaction not only depends on the local contact between the APPJ and the target, but is also closely related to the global discharge characteristics.

3.3 Feedback of surface charge on APPJ-target interaction

When the polarity of σ reverses, the discharge properties change accordingly. Figure 11 presents the temporal evolution of the radial electric field component E_r above the target (with a distance of 10 μm) and surface charge density σ on the target. E_r is positive as pointing outward.

As for case 1, the induced SIW starts to propagate in the radial direction, and the fields at locations further away from the central region sequentially reach the peak and then diminish after the front passes. As the voltage reduces, the peak amplitude of E_r drastically drops, and the positive SIW stops near r = 1.5 mm. After the pulse end, the surface charge density gradually decreases and changes its polarity to negative at ~46.1 ns.

However, after the instant of E polarity reverse in the central region (47 ns for case 2 and 36.8 ns for case 3), a negative SIW further develops along the target surface, forming a diffuse profile at the periphery and contacting the target directly. During this process, the direction of E_r reverses by pointing inwards, and n_e in the discharge channel is obviously elevated, indicating that the SIW transforms from the positive to the negative one. This also explains the time lag of σ polarity reverse between the central and periphery regions (figure 6).

As reported in reference [26,34], the charging process occurs faster in the center of the impact point, which is proved in this work that the surface charge in the inner region firstly transits from positive to negative polarity, and then gradually expands outward along the target surface. This non-uniform distribution of surface charge causes a remarkable radial component of electric field and induces a negative SIW further develops, which results in the direction of E_r revert. The mechanism causes the polarity reversion of surface charge at diverse locations are different. In the center region, it is attributed to the reversal of electric field caused by the extension of forward stroke, whereas in

the outer region, it is due to the continuous propagation of negative SIW.

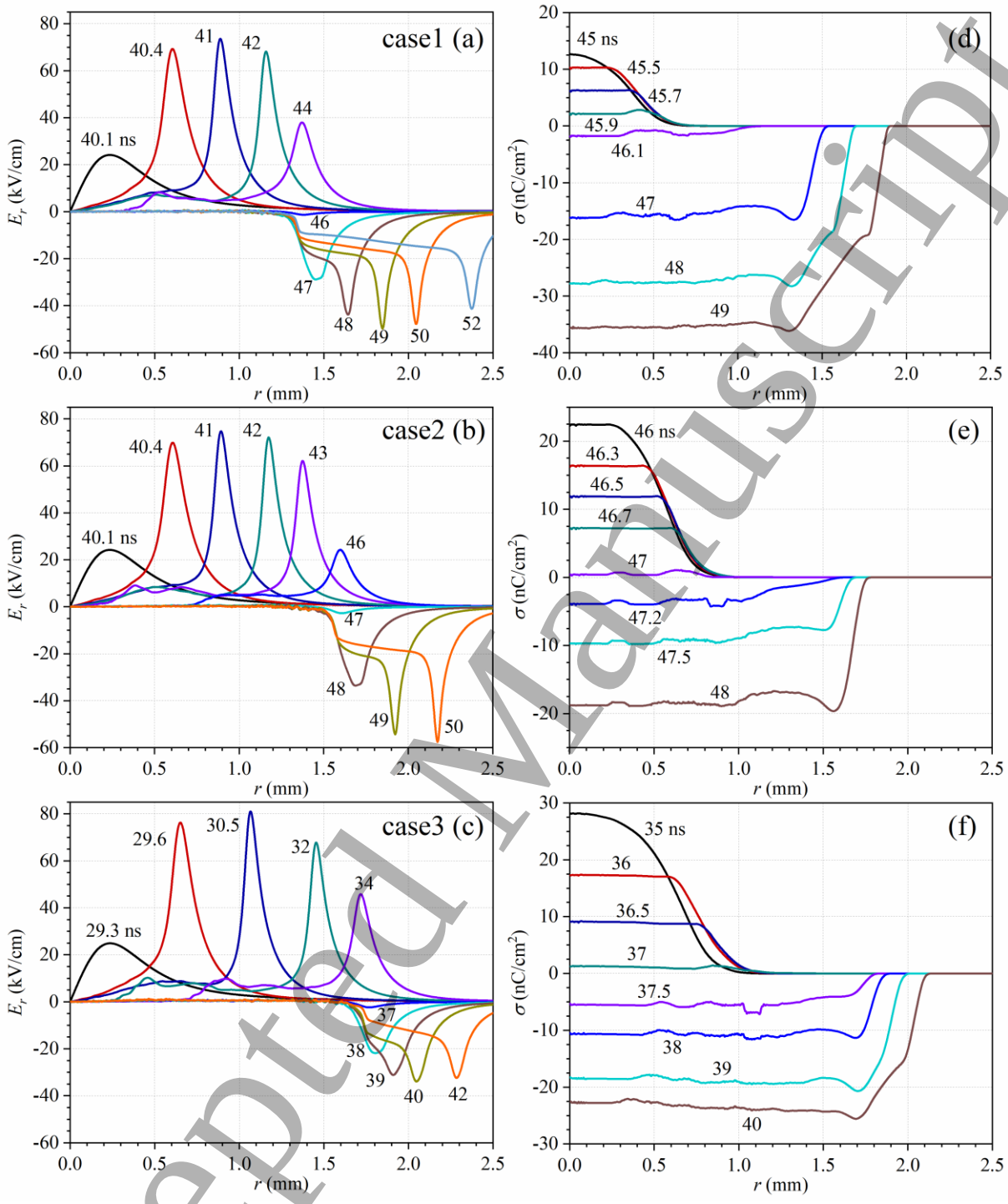

Figure 11. Temporal evolution of the radial component of electric field E_r (left column) and the surface charge σ (right column) on the target with different cases. The E_r data is selected at the position with a distance of 10 μm above the target.

To clarify how the surface charge dynamic affects the APPJ-surface interaction, the comparison

of the total charge accumulation Q, the net charge transfer, and the properties of energy deposition for different pulses are shown in figure 12. The obtained net charge transfer and total energy is integrated over the voltage pulse. The energy deposition means the integration of power density due to electron Joule heating. This can be thought of the total energy that electrons can get from the applied electric field, which then consumed in the collisions such as excitation and ionization. Thus, the coverage of the energy deposition can be used to roughly represent the spatial distribution of active species, which may play a key role in the plasma-surface interaction.

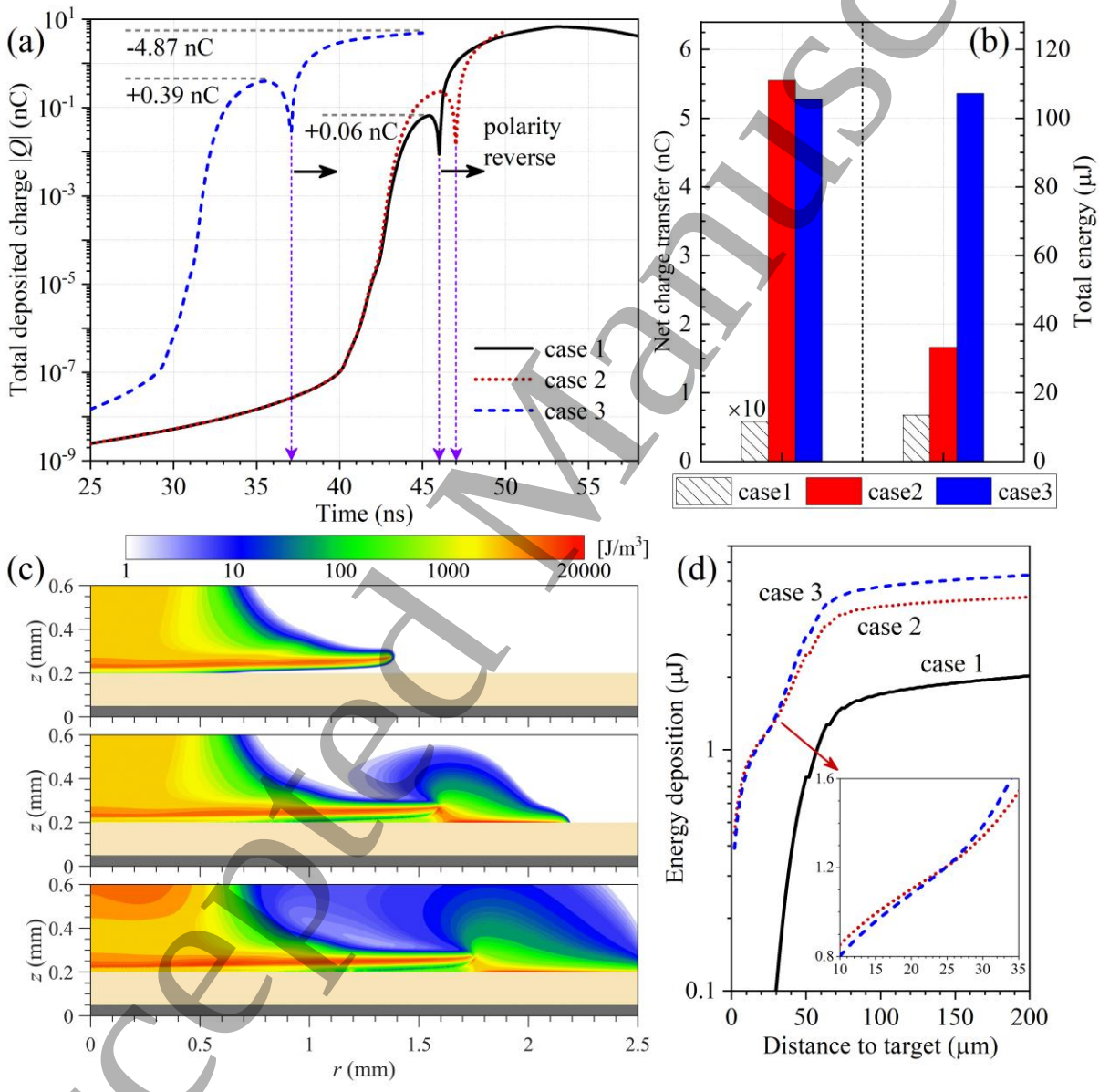

Figure 12. (a) Temporal evolution of the total deposited surface charge on the target, (b) the net charge transfer and total energy during the voltage pulse, (c) spatial distribution of the energy density, and (d) energy deposited near the target for different voltage waveforms. Dashed lines with

arrow indicate the instant of polarity reverse for Q.

The amplitude of Q first reaches the peak (positive) during the propagation of SIW, and then sharply changes its polarity and increases in the opposite direction (negative) until the pulse ends. The difference between the two peaks within the voltage pulse is defined as the net charge transfer, which is generally considered to be correlated with the energy deposition during the discharge pulse [22,23]. The maximal net charge transfer in this work can reach up to ~5.3 nC, which is at the same order of magnitude with the typical value measured in experiments [63].

The spatial distribution of energy deposition can be obtained by firstly summing the product of energy density and cell volume over the computation domain, and then integrating it over the voltage pulse. As shown in figure 12(c), the spatial coverage and the energy density vary among the three pulses. For example, more energy is deposited near the surface in cases 2 and 3 with σ polarity reverse due to the further developed SIW or the enhanced discharge in space with higher voltage amplitude, respectively.

Intuitively, the closer to the target, the greater dominant role of the deposited energy is likely to be in the plasma-surface interaction. However, by summing the energy deposition over a certain distance, the obtained total energy as a function of the distance to the target surface shows a different tendency (figure 12(d)). It is found that in regions closer to the target (with a distance of ~24 μm), the deposited energy in case 2 has a larger magnitude than that of case 3, which is exactly consistent with that of the net charge transfer. But further away from the surface, the trend is reversed, suggesting that the energy provided by the discharge in space begins to dominate due to the elevated voltage amplitude. For practical applications, the net charge transfer can be used to evaluate the energy deposition between the APPJ-surface interaction quantitatively.

The results demonstrate the impact of forward strokes on the surface charge dynamics and the feedback effect of σ on the development and energy deposition of the discharge, revealing the fundamental process of the plasma-surface interaction under the positive pulses. In fact, the interaction between the APPJ and the dielectric target is essentially a 3D phenomenon, which makes it difficult to capture the complex dynamics of the discharge propagation by the 2D axisymmetric fluid model, such as the stochastic branching or the plasma pattern formed on the surface [64]. The

2D axisymmetric fluid model is suitable to treat the axial dominance problem, such as the discharge in a pin-to-plate electrode. Inevitably, the more deviation of discharge morphology from the axisymmetric structure, the less accuracy of the simulation compared to the reality. However, at present, the 2D model is still an effective method to fairly good describe the discharge dynamics with less computational burden. It should be noted that the parameter sweep considered in this work is quite limited, which only reveals the critical thresholds of parameters that affect the surface charge dynamics, *e.g.* a higher voltage amplitude or a longer pulse width can lead to earlier polarity reversal of the surface charge. The investigations on more detailed parameter sweep are beyond the scope of this work. In addition, the photoionization model for the Ar/air discharge developed in this work is still rough and needs further precise verification in experiments. A kinetic treatment of electrons or a 3D model is required to advance the understanding of the plasma-surface interaction.

4. Conclusions

In this work, the interaction of a nanosecond pulsed atmospheric pressure plasma jet with a grounded dielectric target is numerically investigated by a 2D axisymmetric fluid model. The development of the APPJ both in the space and on the target is obtained under different pulse parameters. The decisive role of forward stroke on the surface charge dynamics, and in turn, the feedback of surface charge on the discharge kinetics and energy deposition in the APPJ-surface interaction are illustrated.

The development of APPJ can be divided into three stages: primary discharge, return and forward strokes, and the SIW on the target. After the primary discharge impact the grounded target, two strokes appear, which first propagates from the target to the powered electrode (return stroke) and then reverses its direction and further develops to target again (forward stroke), creating the conditions for field reversal near the target. The forward stroke, characterized by an elevated electric field with a relatively uniform distribution across the plasma column, has a decisive impact on the direction of the axial electric field near the target. By extending the pulse width or elevating the voltage amplitude, the forward stroke is enhanced and the potential drop across the plasma column can exceed the applied voltage, which reverts the direction of electric field and promotes the motion of electrons towards the target. Ultimately, the polarity of surface charges on the target is reversed.

Although this work only focuses on a limited range of the parameter sweep, the revealed mechanism is also applicable to the phenomenon that the polarity reversal of surface charge observed under different electrode structures and voltage waveforms like in references [23,25,33-36]. Specifically, as the potential drop across the plasma column exceeds the applied voltage, the resulting direction reversal of electric field can affect the polarity of surface charge. The simulated results elucidate the impact of this competitive relation on the surface charge dynamics.

Due to the time sequence of the polarity reverse of surface charges along the radial positions, a remarkable radial component of the electric field is induced, resulting in a negative SIW further develops on the target surface. Furthermore, the energy deposition in the vicinity of the target is significantly enhanced, which is positively correlated with the net charge transfer on the dielectric. The presented work demonstrates the relationship between the pulse parameters, discharge kinetics, and surface charge dynamics, providing insight into the regulation of the energy deposition in the plasma-surface interaction and the optimization of APPJ applications.

Data availability statement

All data that support the findings of this study are included within the article (and any supplementary files)

Acknowledgments

This work was supported by the National Natural Science Foundation of China (Grant Nos. 52350072, 52437007, 52277167), Beijing Nova Program (Grant No. 20240484512), and Beijing Natural Science Foundation (Grant No. 1242030). The authors are thankful to Dr. Yifei Zhu for kindly providing simulation resources.

Appendix

(1) Basic equations and flux boundary

$$\frac{\partial n}{\partial t} + \nabla \cdot \boldsymbol{\Gamma} = S \tag{A1}$$

$$\boldsymbol{\Gamma} = n\boldsymbol{u} = -D\nabla n + \mu \boldsymbol{E} n \tag{A2}$$

$$\frac{\partial\left(n_e\varepsilon_m\right)}{\partial t}+\nabla\cdot\boldsymbol{\Gamma}_\varepsilon=-\left|q_e\right|\cdot\boldsymbol{E}\cdot\boldsymbol{\Gamma}_e-P\left(\varepsilon_m\right) \tag{A3}$$

$$\nabla\left(\varepsilon_0\varepsilon_r\nabla\phi\right)=-\rho-\sigma \tag{A4}$$

$$\frac{\partial\sigma}{\partial t}=\sum_i q_i\left(-\nabla\cdot\boldsymbol{\Gamma}_i\right) \tag{A5}$$

where n, $\boldsymbol{\Gamma}$, S, D, and μ are number density, flux, source term due to reactions or photoionization, diffusion coefficient, and mobility of species. n_e, q_e, ε_m, $\boldsymbol{\Gamma}_\varepsilon$ are the electron density, elementary charge, mean electron energy, flux term, respectively. Electron transport coefficients, reaction rates, and electron collision power lost $P(\varepsilon_m)$ are calculated by Bolsig+ [55], based on the local mean energy approximation (LMEA). Poisson equation is solved with consideration of the dielectric surface charge density σ. In the simulation, the initial value of mean electron energy is set a low value 1 eV, and the surface charge density is zero.

The boundary condition that the species flux $\boldsymbol{\Gamma}$ to be directed towards the surface is imposed in the model according to [65-67],

$$\boldsymbol{\Gamma}_e\cdot\boldsymbol{n}_s=\left(a-1\right)\mu_e n_e\boldsymbol{E}\cdot\boldsymbol{n}_s-\left(a-1\right)D_e\nabla n_e\cdot\boldsymbol{n}_s-a\sum\gamma\boldsymbol{\Gamma}_{i,+}\cdot\boldsymbol{n}_s \tag{A6}$$

$$\boldsymbol{\Gamma}_\varepsilon\cdot\boldsymbol{n}_s=\left(a-1\right)\mu_\varepsilon n_e\varepsilon_m\boldsymbol{E}\cdot\boldsymbol{n}_s-\left(a-1\right)D_\varepsilon\nabla n_e\varepsilon_m\cdot\boldsymbol{n}_s-a\left(\frac{5}{2}k_bT_{se}\right)\sum\gamma\boldsymbol{\Gamma}_{i,+}\cdot\boldsymbol{n}_s \tag{A7}$$

$$\boldsymbol{\Gamma}_{i,-}\cdot\boldsymbol{n}_s=\left(a-1\right)\mu_{i,-}n_{i,-}\boldsymbol{E}\cdot\boldsymbol{n}_s-\left(a-1\right)D\nabla n_{i,-}\cdot\boldsymbol{n}_s \tag{A8}$$

$$\boldsymbol{\Gamma}_{i,+}\cdot\boldsymbol{n}_s=a\mu_{i,+}n_{i,+}\boldsymbol{E}\cdot\boldsymbol{n}_s-aD_{i,+}\nabla n_{i,+}\cdot\boldsymbol{n}_s \tag{A9}$$

$$a=\begin{cases}1, & \boldsymbol{E}\cdot\boldsymbol{n}_s<0\\ 0, & \boldsymbol{E}\cdot\boldsymbol{n}_s\geq 0\end{cases} \tag{A10}$$

where $\boldsymbol{\Gamma}_e$, $\boldsymbol{\Gamma}_\varepsilon$, $\boldsymbol{\Gamma}_{i,-}$, $\boldsymbol{\Gamma}_{i,+}$ are the flux of electron, electron energy, negative, and positive species. $\boldsymbol{n}_s$ is normal vector pointing outward. γ is the secondary emission coefficient by impact of ions. T_{se} are the temperature of electron of secondary electron emitted from surface, and is set as 1 eV in the simulation [67].

In the simulation, an adaptive time step is used. The time step is limited by four characteristic time scales [68]: the drift dynamics time step Δt_{CFLE}, the diffusion dynamics time step Δt_{DiffE}, the

kinetics time step Δt_{KinE}, and the dielectric relaxation time step Δt_{DielRT}.

$$\Delta t_{CFLE} = \min\left[\frac{\Delta x_i}{v_x(i,j)}, \frac{\Delta y_i}{v_y(i,j)}\right] \tag{A11}$$

$$\Delta t_{DiffE} = \min\left[\frac{(\Delta x_i)^2}{D_x(i,j)}, \frac{(\Delta y_i)^2}{D_y(i,j)}\right] \tag{A12}$$

$$\Delta t_{KinE} = \min\left[\frac{n_e(i,j)}{S_{kin}(i,j)}\right] \tag{A13}$$

$$\Delta t_{DielRT} = \min\left[\frac{\varepsilon_0}{q_e \mu_e(i,j) n_e(i,j)}\right] \tag{A14}$$

$$\Delta t = \min\left(\xi_{CFL}\Delta t_{CFLE}, \xi_{Diff}\Delta t_{DiffE}, \xi_{Kin}\Delta t_{KinE}, \xi_{Diel}\Delta t_{DielRT}\right) \tag{A15}$$

where, ξ_{CFL}=0.1, ξ_{Diff}=0.1, ξ_{Kin}=1.0, ξ_{Diel}=1.0. During the simulation, the timestep ranges from ~10^{-14} to ~10^{-12} s and is minimum after the discharge impact the grounded dielectric target, which is small enough to avoid affecting the results.

(2) Photoionization for Ar/air system

A photoionization model for discharge in the argon/air mixture is developed to study the APPJ properties. It assumes that the VUV radiation emitted by the excited argon species is absorbed by O_2 and photoionization occurs. The photoionization rate S_{ph} at point r due to source point r' emitting UV photons can be written as [69,70],

$$S_{ph}(\boldsymbol{r}) = \iiint_V \frac{I_r \cdot g(R)}{4\pi R^2} dV = Ap \iiint_V \frac{\xi n(r')}{\tau} \frac{\exp(-\lambda p R)}{4\pi R^2} dV \tag{A11}$$

where R is the distance between the two points r and r'. I, p, ξ, n, and τ are the photon source term, the total pressure, the photoionization efficiency, the density and lifetime of the excited state, respectively. The photoionization function takes the following form [70,71],

$$\frac{g(R)}{p} = Ae^{-\lambda p R} \tag{A12}$$

$$\frac{g(R)}{p} = \frac{1}{4\pi} \frac{\omega}{\alpha_{eff}} \frac{\int_{\lambda_{\min}}^{\lambda_{\max}} \xi_\lambda (\mu_\lambda / p) \mathrm{e}^{-(\mu_\lambda / p) p R} I_\lambda d\lambda}{\int_{\lambda_{\min}}^{\lambda_{\max}} I_\lambda d\lambda} \tag{A13}$$

where ω is the excitation coefficient of emitting state, α_{eff} is the effective Townsend coefficient. $\lambda_{\min}$ and $\lambda_{\max}$ is the spectral range of the radiation. ξ_λ and μ_λ are the spectrally resolved photoionization yield and the absorption coefficient.

As a rough approximation, several spectral lines are selected to implement the multigroup method [69], and then substitute the complex spectral integration term in equation 4, which corresponds to the lower energy bound for O_2 ionization (12.06 eV, 102.8 nm), the upper bound for N_2 ionization (15.6 eV, 79.7 nm), and that having the strongest intensity (87.9 nm) within this range [72], respectively. Specifically, for each component *j*, the equation 4 can be simplified,

$$\frac{g(R)}{p} = \sum_j \frac{1}{4\pi} \frac{\omega}{\alpha_{eff}} \xi_{\lambda,j} \frac{\mu_\lambda}{p} \mathrm{e}^{-(\mu\lambda/p)pR} \tag{A14}$$

By comparing equation 3, the fitting parameters A_j and λ_j can be evaluated, and photoionization rate $S_{ph,j}$ can be obtained,

$$A_j = \frac{1}{4\pi} \frac{\omega}{\alpha_{eff}} \xi_{\lambda,j} \frac{\mu_\lambda}{p} \tag{A15}$$

$$\lambda_j = \frac{\mu_{\lambda,j}}{p} = \sigma_{abs,j} \frac{1}{k_B T} \tag{A16}$$

$$\left[\nabla^2 - 3\left(\lambda_j p\right)^2\right]\left[\xi\psi_{0,j}(r)\right] = -3\lambda_j p\xi \frac{n(r)}{c\tau} \tag{A17}$$

$$S_{ph}(r) = \sum_j S_{ph,j}(r) = \sum_j A_j pc\psi_{0,j}(r) \tag{A18}$$

where k_B is the Boltzmann constant, T is the gas temperature, c is the light speed, and $\Psi_0(r)$ is the isotropic part of the photon distribution function. σ_{abs} is the absorption cross section with the value of 1.1×10^{18} cm^{-2} (102.5 nm), 11.58×10^{18} cm^{-2} (87.9 nm), and 23.1×10^{18} cm^{-2} (79.7 nm) for each component [73], respectively. Although the rough treatment proposed in this work falls short of physics to some extent, it still provides a feasible approximation to access the photoionization for discharges in the Ar/air mixture.

(3) Validity of the drift-diffusion approximation

As reported in reference [74], the requirement for validity of the drift-diffusion approximation is $\Lambda_{ch} \gg \lambda_{mfp}$, where λ_{mfp} is the mean free path of electron, and Λ_{ch} is the spatial scale of electron density variation in the streamer head. Considering the Ar/air mixture of APPJ system in this work, the effective cross section should range from 3×10^{-20} m^2 (N_2 molecule) [74] to 10^{-19} m^2 (Ar molecule) [56] and the neutral gas density at atmospheric pressure is ~2.5×10^{25} m^{-3}, resulting in λ_{mfp} is about 0.4-1.3 μm. The distribution of electron density after the impact of discharge on the target is shown as an example for the calculation of Λ_{ch} with conditions of case 3 V_a = 10 kV and W_p = 35 ns (figure A1). It can be found that Λ_{ch} sharply decreases as the discharge approaches the target and the minimum is ~7.9 μm, which is still far larger than λ_{mfp}. Besides, the electric field in streamer head E_{sh} only slightly rises above the critical limit E_{lim} = 1500 Td [74] and then reduces to a low value. Thus, it can be generally regarded that the setting of mesh size and timestep in the simulation is able to describe this APPJ system.

$$\Lambda_{ch}^{-1} = \frac{1}{n_e}\frac{\mathrm{d}n_e}{\mathrm{d}x} \tag{A19}$$

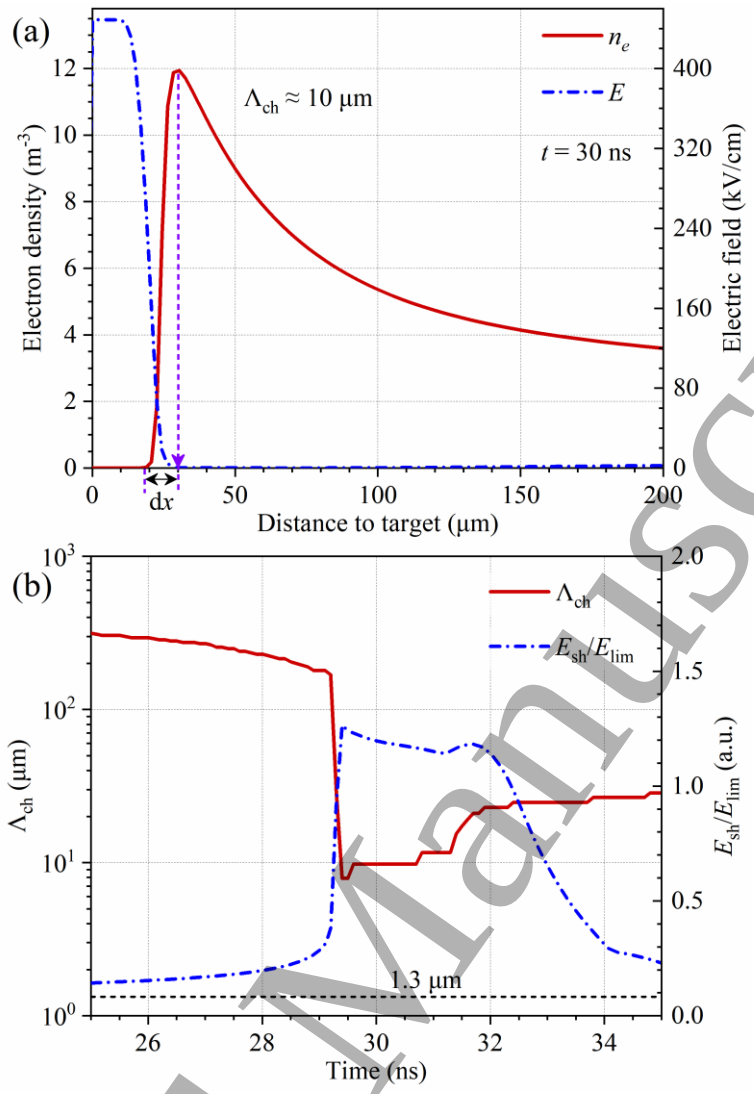

Figure A1. (a) Illustration for calculating the spatial scale of electron density variation in the streamer head Λ_{ch}, (b) temporal evolution of Λ_{ch} and ratio of E_{sh}/E_{lim}.

(4) Impact of mesh size

A refiner mesh with size of 1 μm is used at the gas-target interface to test the impact of mesh size on the simulation results. The spatial and temporal evolution of surface charge on the grounded target and the dynamics of $|\sigma|$ at different locations along the path of SIW are given in figure A2. It can be found that the revert instant is slightly delayed but the phenomenon of the polarity reverse for the surface charge remains unchanged. This also indicates that the mesh size of 2 μm is enough to capture the reversal of surface charge at the gas-target interface.

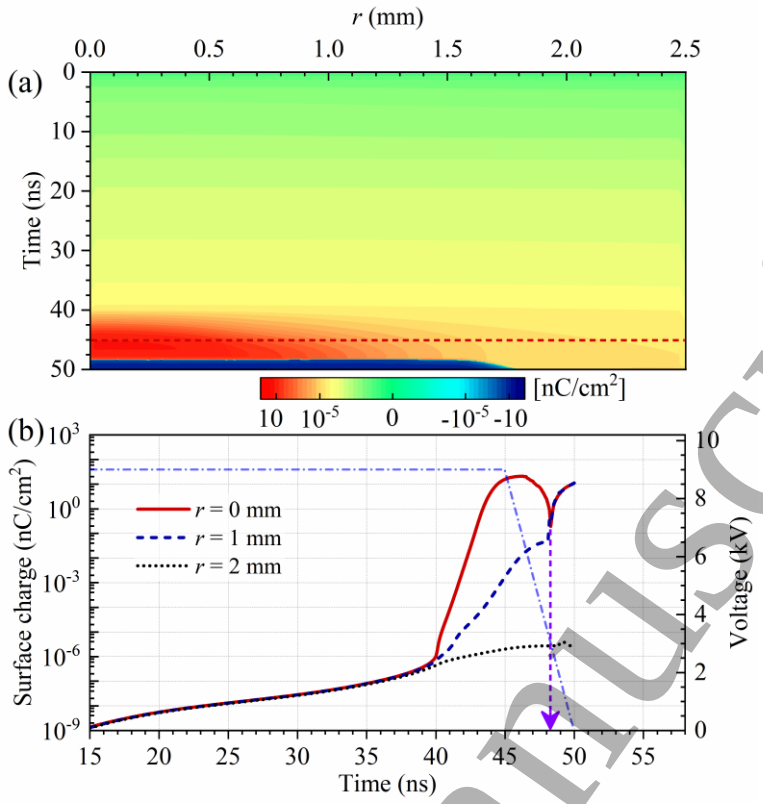

Figure A2. Spatial and temporal evolution of the surface charge σ on the grounded target and dynamics of $|\sigma|$ at different locations along the path of SIW. Dashed lines with arrow indicate the instant of polarity reverse for σ. Conditions: case 2, V_a = 9 kV and W_p = 40 ns, mesh size is 1 μm at the gas-target interface.

(5) Impact of secondary electron emission

A lower γ of 0.01 is used to test the impact of secondary electron emission coefficient on the simulation results. The spatial and temporal evolution of surface charge on the grounded target and the dynamics of $|\sigma|$ at different locations along the path of SIW are given in figure A3. The instant of the surface charge polarity reversal appears earlier (~46.3 ns) compared to case with a larger secondary electron emission coefficient γ = 0.1 (~47 ns, figure 6(b)). However, the phenomenon of the surface charge reversal can still be captured.

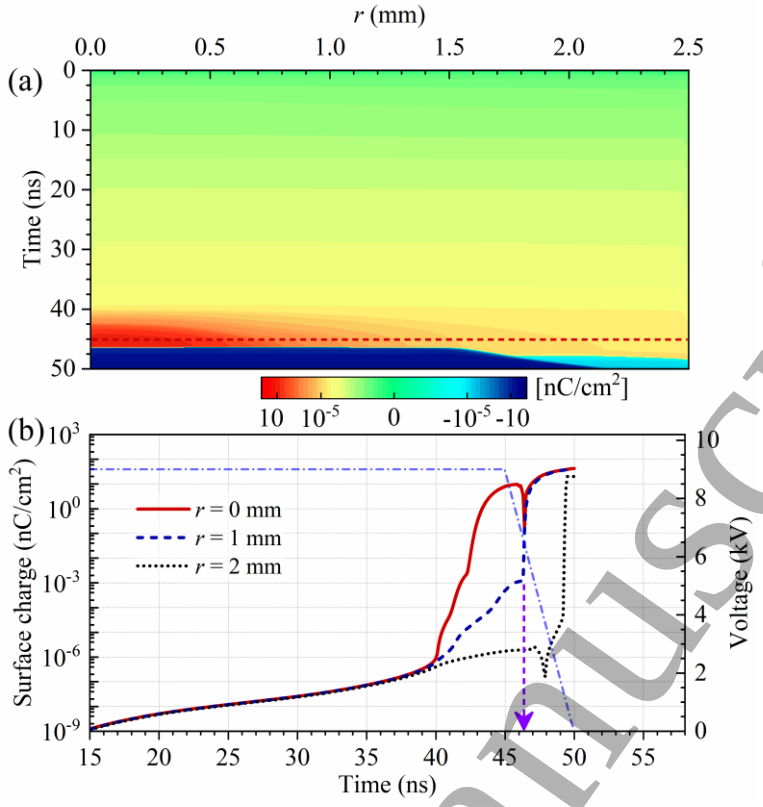

Figure A3. Spatial and temporal evolution of the surface charge σ on the grounded target and dynamics of $|\sigma|$ at different locations along the path of SIW. Dashed lines with arrow indicate the instant of polarity reverse for σ. Conditions: case 2, V_a = 9 kV and W_p = 40 ns, secondary electron emission is 0.01.

(6) Reaction scheme for Ar/Air mixture

Table A1 Kinetics scheme of $Ar/N_2/O_2$ system in APPJ [51-54]

No.	Reactions	Rate (s^{-1}, cm^3s^{-1}, cm^6s^{-1})
1	$e + N_2 \rightarrow e + e + N_2^+$	$f(\varepsilon)$
2	$e + O_2 \rightarrow e + e + O_2^+$	$f(\varepsilon)$
3	$e + N_2 \rightarrow e + e + N_2(A^3\Sigma_u^+)$	$f(\varepsilon)$
4	$e + N_2 \rightarrow e + e + N_2(B^3\Pi_g)$	$f(\varepsilon)$
5	$e + N_2 \rightarrow e + e + N_2(C^3\Pi_u)$	$f(\varepsilon)$
6	$e + O_2 \rightarrow e + O + O$	$f(\varepsilon)$
7	$e + O_2 \rightarrow e + O + O(^1D)$	$f(\varepsilon)$
8	$N_2^+ + N_2 + N_2 \rightarrow N_4^+ + N_2$	$5 \cdot 10^{-29}$
9	$N_2^+ + N_2 + O_2 \rightarrow N_4^+ + O_2$	$5 \cdot 10^{-29}$

No.	Reactions	Rate (s^{-1}, cm^3s^{-1}, cm^6s^{-1})
10	$N_4^+ + O_2 \rightarrow O_2^+ + N_2 + N_2$	$2.5 \cdot 10^{-10}$
11	$N_2^+ + O_2 \rightarrow O_2^+ + N_2$	$6 \cdot 10^{-11}$
12	$O_2^+ + N_2 + N_2 \rightarrow O_2^+N_2 + N_2$	$9 \cdot 10^{-31}$
13	$O_2^+N_2 + N_2 \rightarrow O_2^+ + N_2 + N_2$	$4.3 \cdot 10^{-10}$
14	$O_2^+N_2 + O_2 \rightarrow O_4^+ + N_2$	10^{-9}
15	$O_2^+ + O_2 + N_2 \rightarrow O_4^+ + N_2$	$2.4 \cdot 10^{-30}$
16	$O_2^+ + O_2 + O_2 \rightarrow O_4^+ + O_2$	$2.4 \cdot 10^{-30}$
17	$e + O_2 + O_2 \rightarrow O_2^- + O_2$	$2 \cdot 10^{-29} \left(300 / T_e\right)$
18	$e + O_2 \rightarrow O^- + O_2$	$f\left(\varepsilon\right)$
19	$O^- + O \rightarrow e + O_2$	$1.4 \cdot 10^{-10}$
20	$O_2^- + O \rightarrow e + O_2 + O$	$1.5 \cdot 10^{-10}$
21	$e + N_4^+ \rightarrow N_2 + N_2\left(C^3\Pi_u\right)$	$2.3 \cdot 10^{-6} \left(300 / T_e\right)^{0.53}$
22	$e + N_2^+ \rightarrow N + N$	$1.8 \cdot 10^{-7} \left(300 / T_e\right)^{0.39}$
23	$e + O_4^+ \rightarrow O + O + O_2$	$1.4 \cdot 10^{-6} \left(300 / T_e\right)^{0.5}$
24	$e + O_2^+ \rightarrow O + O$	$2 \cdot 10^{-7} \left(300 / T_e\right)$
25	$O_2^- + O_4^+ \rightarrow 3O_2$	10^{-7}
26	$O_2^- + O_4^+ + N_2 \rightarrow 3O_2 + N_2$	$2 \cdot 10^{-25}$
27	$O_2^- + O_4^+ + O_2 \rightarrow 3O_2 + O_2$	$2 \cdot 10^{-25}$
28	$O_2^- + O_2^+ + N_2 \rightarrow 2O_2 + N_2$	$2 \cdot 10^{-25}$
29	$O_2^- + O_2^+ + O_2 \rightarrow 2O_2 + O_2$	$2 \cdot 10^{-25}$
30	$O^- + N_2^+ \rightarrow O + N + N$	$2 \cdot 10^{-7} \left(300 / T_{gas}\right)^{0.5}$
31	$N_2\left(C^3\Pi_u\right) + N_2 \rightarrow N_2\left(B^3\Pi_g\right) + N_2$	10^{-11}
32	$N_2\left(C^3\Pi_u\right) + O_2 \rightarrow N_2 + O + O\left(^1D\right)$	$3 \cdot 10^{-10}$
33	$N_2\left(C^3\Pi_u\right) \rightarrow N_2 + h\nu$	$2.45 \cdot 10^7$
34	$N_2\left(B^3\Pi_g\right) + O_2 \rightarrow N_2 + O + O$	$3 \cdot 10^{-11}$
35	$N_2\left(B^3\Pi_g\right) + N_2 \rightarrow N_2\left(A^3\Sigma_u^+\right) + N_2$	10^{-11}
36	$N_2\left(A^3\Sigma_u^+\right) + O_2 \rightarrow N_2 + O + O$	$2.5 \cdot 10^{-12} \left(T_{gas} / 300\right)^{0.5}$
37	$O\left(^1D\right) + O_2 \rightarrow O + O_2$	$3.3 \cdot 10^{-11} \exp\left(67 / T_{gas}\right)$
38	$O\left(^1D\right) + N_2 \rightarrow O + N_2$	$1.8 \cdot 10^{-11} \exp\left(107 / T_{gas}\right)$
39	$e + Ar \rightarrow e + e + Ar^+$	$f\left(\varepsilon\right)$
40	$e + Ar \rightarrow e + Ar\left(1s_5\right)$	$f\left(\varepsilon\right)$
41	$e + Ar \rightarrow e + Ar\left(1s_2\right)$	$f\left(\varepsilon\right)$
42	$e + Ar \rightarrow e + Ar\left(2p_1\right)$	$f\left(\varepsilon\right)$

No.	Reactions	Rate (s^{-1}, cm^3s^{-1}, cm^6s^{-1})
43	$e + Ar(1s_5) \rightarrow e + e + Ar^+$	$f(\varepsilon)$
44	$e + Ar(1s_5) \rightarrow e + Ar$	$2 \cdot 10^{-7} \cdot 0.4$
45	$e + Ar(1s_2) \rightarrow e + Ar$	$2 \cdot 10^{-7} \cdot 0.4$
46	$e + Ar(2p_1) \rightarrow e + Ar$	$2 \cdot 10^{-7} \cdot 0.2$
47	$e + Ar(1s_5) \rightarrow e + Ar(1s_2)$	$f(\varepsilon)$
48	$e + Ar(1s_2) \rightarrow e + Ar(2p_1)$	$f(\varepsilon)$
49	$e + e + Ar^+ \rightarrow e + Ar(2p_1)$	$2 \cdot 10^{-20} (300 / T_e)^{4.5}$
50	$e + Ar^+ + Ar \rightarrow Ar(2p_1) + Ar$	$6 \cdot 10^{-29}$
51	$e + Ar_2^+ \rightarrow Ar(1s_5) + Ar$	$1.62 \cdot 10^{-7} (300 / T_e)^{0.64} \cdot 0.4$
52	$e + Ar_2^+ \rightarrow Ar(1s_2) + Ar$	$1.62 \cdot 10^{-7} (300 / T_e)^{0.64} \cdot 0.4$
53	$e + Ar_2^+ \rightarrow Ar(2p_1) + Ar$	$1.62 \cdot 10^{-7} (300 / T_e)^{0.64} \cdot 0.2$
54	$Ar + Ar(2p_1) \rightarrow Ar + Ar(1s_5)$	$4 \cdot 10^{-11}$
55	$Ar + Ar + Ar^+ \rightarrow Ar + Ar_2^+$	$2.5 \cdot 10^{-31}$
56	$Ar + Ar_2^* \rightarrow Ar + Ar + Ar(2p_1)$	10^{-12}
57	$Ar(1s_5) + Ar(1s_5) \rightarrow e + Ar + Ar^+$	$1.62 \cdot 10^{-10}$
58	$Ar(1s_2) + Ar(1s_2) \rightarrow e + Ar + Ar^+$	$1.62 \cdot 10^{-10}$
59	$Ar(2p_1) + Ar(2p_1) \rightarrow e + Ar + Ar^+$	$1.62 \cdot 10^{-10}$
60	$Ar(1s_5) + Ar(2p_1) \rightarrow e + Ar + Ar^+$	$1.62 \cdot 10^{-10}$
61	$Ar(1s_2) + Ar(2p_1) \rightarrow e + Ar + Ar^+$	$1.62 \cdot 10^{-10}$
62	$Ar(1s_5) + Ar_2^* \rightarrow e + 2Ar + Ar^+$	$6 \cdot 10^{-10}$
63	$Ar(1s_2) + Ar_2^* \rightarrow e + 2Ar + Ar^+$	$6 \cdot 10^{-10}$
64	$Ar(1s_5) + Ar + Ar \rightarrow Ar_2^* + Ar$	10^{-32}
65	$Ar_2^* + Ar_2^* \rightarrow e + 2Ar + Ar_2^+$	$5 \cdot 10^{-10}$
66	$Ar(1s_2) \rightarrow Ar$	$5 \cdot 10^{8}$
67	$Ar(1s_2) \rightarrow Ar$	$4.2 \cdot 10^{7}$
68	$Ar_2^* \rightarrow 2Ar$	$3.8 \cdot 10^{6}$
69	$Ar(1s_5) + O_2 \rightarrow Ar + O + O$	$2.1 \cdot 10^{-10}$
70	$Ar(1s_5) + N_2 \rightarrow Ar + N_2(A^3\Sigma_u^+)$	$3.6 \cdot 10^{-11}$
71	$Ar(1s_5) + N_2 \rightarrow Ar + N + N$	$3.6 \cdot 10^{-11}$
72	$Ar(1s_5) + N_2(A^3\Sigma_u^+) \rightarrow Ar + N_2^+ + e$	$5 \cdot 10^{-10}$
73	$Ar(1s_5) + N_2(A^3\Sigma_u^+) \rightarrow Ar + N + N$	$3.6 \cdot 10^{-11}$
74	$Ar(1s_2) + O_2 \rightarrow Ar + O + O$	$2.1 \cdot 10^{-10}$
75	$Ar(1s_2) + N_2 \rightarrow Ar + N_2(A^3\Sigma_u^+)$	$3.6 \cdot 10^{-11}$

No.	Reactions	Rate (s^{-1}, cm^3s^{-1}, cm^6s^{-1})
76	$Ar(1s_2) + N_2 \rightarrow Ar + N + N$	$3.6 \cdot 10^{-11}$
77	$Ar(1s_2) + N_2(A^3\Sigma_u^+) \rightarrow Ar + N_2^+ + e$	$5 \cdot 10^{-10}$
78	$Ar(1s_2) + N_2(A^3\Sigma_u^+) \rightarrow Ar + N + N$	$3.6 \cdot 10^{-11}$
79	$Ar(2p_1) + O_2 \rightarrow Ar + O_2$	$7.6 \cdot 10^{-10}$
80	$Ar(2p_1) + O_2 \rightarrow Ar + O + O$	$2.1 \cdot 10^{-10}$
81	$Ar(2p_1) + N_2 \rightarrow Ar + N_2(A^3\Sigma_u^+)$	$3.6 \cdot 10^{-11}$
82	$Ar(2p_1) + N_2 \rightarrow Ar + N + N$	$3.6 \cdot 10^{-11}$
83	$Ar(2p_1) + N_2 \rightarrow Ar + N_2$	$3.2 \cdot 10^{-11}$
84	$Ar^+ + O^- \rightarrow Ar + O$	$2 \cdot 10^{-7}$
85	$Ar^+ + O^- + Ar \rightarrow 2Ar + O$	$2 \cdot 10^{-25}$
86	$Ar^+ + O^- + O_2 \rightarrow Ar + O + O_2$	$2 \cdot 10^{-25}$
87	$Ar^+ + O^- + N_2 \rightarrow Ar + O + N_2$	$2 \cdot 10^{-25}$
88	$Ar^+ + O_2^- \rightarrow Ar + O_2$	$2 \cdot 10^{-7}$
89	$Ar^+ + O_2^- \rightarrow Ar + O + O$	10^{-7}
90	$Ar^+ + O_2^- + Ar \rightarrow 2Ar + O_2$	$2 \cdot 10^{-25}$
91	$Ar^+ + O_2^- + O_2 \rightarrow Ar + 2O_2$	$2 \cdot 10^{-25}$
92	$Ar^+ + O_2^- + N_2 \rightarrow Ar + O_2 + N_2$	$2 \cdot 10^{-25}$
93	$Ar^+ + O_2 \rightarrow Ar + O_2^+$	$5 \cdot 10^{-11}$
94	$Ar^+ + N_2 \rightarrow Ar + N_2^+$	$7 \cdot 10^{-10}$
95	$Ar_2^* + O_2 \rightarrow 2Ar + 2O$	$4.6 \cdot 10^{-11}$
96	$Ar_2^* + N_2 \rightarrow 2Ar + N_2(A^3\Sigma_u^+)$	$1.2 \cdot 10^{-11}$
97	$Ar_2^+ + O^- \rightarrow 2Ar + O$	10^{-7}
98	$Ar_2^+ + O_2 \rightarrow 2Ar + O_2^+$	10^{-10}
99	$Ar_2^+ + O_2^- \rightarrow 2Ar + O_2$	10^{-7}
100	$Ar_2^+ + O_2^- \rightarrow 2Ar + 2O$	10^{-7}
101	$O + O + Ar \rightarrow Ar + O_2$	$5.21 \cdot 10^{-35} \exp(-900 / T_{gas})$
102	$N + N + Ar \rightarrow Ar + N_2$	$1.38 \cdot 10^{-34} \exp(-500 / T_{gas})$
103	$N_2(A^3\Sigma_u^+) + Ar \rightarrow N_2 + Ar$	$4 \cdot 10^{-17}$
104	$N_4^+ + Ar^+ \rightarrow Ar^+ + N_2 + N_2$	10^{-11}

References

1 Park S, Choe W, Lee H, Park J Y, Kim J, Moon S Y, and Cvelbar U 2021 Stabilization of liquid instabilities with ionized gas jets *Nature* **592**, 49–53 DOI: 10.1038/s41586-021-03359-9

2 Adamovich I V, Agarwal S, Ahedo E, *et al*. 2022 The 2022 Plasma Roadmap: low temperature plasma science and technology *J. Phys. D: Appl. Phys.* **55**, 373001 DOI: 10.1088/1361-6463/ac5e1c

3 Babaeva N Y and Naidis G V 2021 Universal nature and specific features of streamers in various dielectric media *J. Phys. D: Appl. Phys.* **54**, 223002 DOI: 10.1088/1361-6463/abe9e0

4 Shao T, Wang R, Zhang C, and Yan P 2018 Atmospheric-pressure pulsed discharges and plasmas: mechanism, characteristics and applications *High Voltage* **3**, 14 DOI: 10.1049/hve.2016.0014

5 Lu X, Naidis G V, Laroussi M, and Ostrikov K 2014 Guided ionization waves: Theory and experiments *Phys. Rep.* **540**, 123-166 DOI: 10.1016/j.physrep.2014.02.006

6 Viegas P, Slikboer E, Bonaventura Z, Guaitella O, Sobota A, and Bourdon A 2022 Physics of plasma jets and interaction with surfaces: review on modelling and experiments *Plasma Sources Sci. Technol*. **31**, 053001 DOI: 10.1088/1361-6595/ac61a9

7 Ghimire B, Szili E J, Lamichhane P, Short R D, Lim J S, Attri P, Masur K, Weltmann K, Hong S, and Choi E H 2019 The role of UV photolysis and molecular transport in the generation of reactive species in a tissue model with a cold atmospheric pressure plasma jet *Appl. Phys. Lett.* **114**, 093701 DOI: 10.1063/1.5086522

8 Konina K, Freeman T A, and Kushner M J 2023 Atmospheric pressure plasma treatment of skin: penetration into hair follicles *Plasma Sources Sci. Technol*. **32**, 085020 DOI: 10.1088/1361-6595/acef59

9 Thirumdas R, Kothakota A, Annapure U, Siliveru K, Blundell R, Gatt R, and Valdramidis V P 2018 Plasma activated water (PAW): Chemistry, physico-chemical properties, applications in food and agriculture *Trends Food Sci. Technol.* **77**, 21-31 DOI: 10.1016/j.tifs.2018.05.007

10 Fanelli F and Fracassi F 2017 Atmospheric pressure non-equilibrium plasma jet technology: general features, specificities and applications in surface processing of materials *Surf. Coat. Technol.* **322**, 174-201 DOI: 10.1016/j.surfcoat.2017.05.027

11 Wang R, Xu H, Zhao Y, Zhu W, Ostrikov K, and Shao T 2019 Effect of dielectric and conductive targets on plasma jet behaviour and thin film properties *J. Phys. D: Appl. Phys.* **52**, 074002 DOI: 10.1088/1361-6463/aaf4c8

12 Lu X, Naidis G V, Laroussi M, Reuter S, Graves D B, and Ostrikov K 2016 Reactive species in non-equilibrium atmospheric-pressure plasmas: Generation, transport, and biological effects *Phys. Rep.* **630**, 1-84 DOI: 10.1016/j.physrep.2016.03.003

13 Wang J and Bruggeman P J 2023 OH density, flux and loss probability measurements in a room temperature atmospheric pressure surface discharge by microscopic laser induced fluorescence *Plasma Sources Sci. Technol*. **32**, 085016 DOI: 10.1088/1361-6595/aceff9

14 Huang B, Zhang C, Sun H, Sorokin D A, Tarasenko V F, and Shao T 2022 Enhancement of hydrogen radical density in atmospheric pressure plasma jet by a burst of nanosecond pulses at 1 MHz *Plasma Sources Sci. Technol*. **31**, 025019 DOI: 10.1088/1361-6595/ac3e3e

15 Babaeva N Y and Naidis G V 2020 Ion energies delivered by negative and positive ionization waves to flat dielectric surfaces *Plasma Sources Sci. Technol*. **29**, 095020 DOI: 10.1088/1361-6595/abb2ea

16 Konina K, Kruszelnicki J, Meyer M E, and Kushner M J 2022 Surface ionization waves propagating over non-planar substrates: wavy surfaces, cut-pores and droplets *Plasma Sources Sci. Technol*. **31**, 115001 DOI: 10.1088/1361-6595/ac9a6c

17 Babaeva N Y and Naidis G V 2022 Splitting of ionization waves at the edge of a dielectric plate oriented at grazing angles between the helium plasma jet and the plate *Plasma Sources Sci. Technol*. **31**, 104004 DOI: 10.1088/1361-6595/ac95c0

18 Babaeva N Y, Naidis G V, Tarasenko V F, Zhang C, Huang B, and Shao T 2021 Interaction of helium plasma jet with tilted targets: consequences of target permittivity, conductivity and incidence angle *Plasma Sources Sci. Technol*. **30**, 115021 DOI: 10.1088/1361-6595/ac3212

19 Klarenaar B L M, Guaitella O, Engeln R, and Sobota A 2018 How dielectric, metallic and liquid targets influence the evolution of electron properties in a pulsed He jet measured by Thomson and Raman scattering *Plasma Sources Sci. Technol*. **27**, 085004 DOI: 10.1088/1361-6595/aad4d7

20 Sobota A, Guaitella O, and Garcia-Caurel E 2013 Experimentally obtained values of electric field of an atmospheric pressure plasma jet impinging on a dielectric surface *J. Phys. D: Appl. Phys.* **46**, 372001 DOI: 10.1088/0022-3727/46/37/372001

21 Yang X, Wang W, Wang X, Du Y, Meng Y, and Wu K 2023 Experimental study of transient surface charging during dielectric barrier discharges in air gap in needle-to-plane geometry *J. Phys. D: Appl. Phys.* **56**, 465202 DOI: 10.1088/1361-6463/acee0a

22 Leonov S B, Petrishchev V and Adamovich I V 2014 Dynamics of energy coupling and thermalization in barrier discharges over dielectric and weakly conducting surfaces on μs to ms time scales *J. Phys. D: Appl. Phys.* **47**, 465201 DOI: 10.1088/0022-3727/47/46/465201

23 Simeni Simeni M, Tang Y, Frederickson K and Adamovich I V 2018 Electric field distribution in a surface plasma flow actuator powered by ns discharge pulse trains *Plasma Sources Sci. Technol.* **27** 104001 DOI: 10.1088/1361-6595/aae1c8

24 Huang B D, Zhang C, Adamovich I V, Akishev Y and Shao T 2020 Surface ionization wave propagation in the nanosecond pulsed surface dielectric barrier discharge: the influence of dielectric material and pulse repetition rate *Plasma Sources Sci. Technol.* **29** 044001 DOI: 10.1088/1361-6595/ab7854

25 Viegas P, Slikboer E, Bonaventura Z, Garcia-Caurel E, Guaitella O, Sobota A, and Bourdon A 2022 Quantification of surface charging memory effect in ionization wave dynamics *Sci. Rep.* **12**, 1181 DOI: 10.1038/s41598-022-04914-8

26 Slikboer E, Viegas P, Bonaventura Z, Garcia-Caurel E, Sobota A, Bourdon A, and Guaitella O 2019 Experimental and numerical investigation of the transient charging of a dielectric surface exposed to a plasma jet *Plasma Sources Sci. Technol.* **28**, 095016 DOI: 10.1088/1361-6595/ab3c27

27 Viegas P, Slikboer E, Obrusnik A, Bonaventura Z, Sobota A, Garcia-Caurel E, Guaitella O, and Bourdon A 2018 Investigation of a plasma-target interaction through electric field characterization examining surface and volume charge contributions: modeling and experiment *Plasma Sources Sci. Technol*. **27**, 094002 DOI: 10.1088/1361-6595/aadcc0

28 Stollenwerk L. Laven J G, and Purwins H G 2007 Spatially resolved surface-charge measurement in a planar dielectric-barrier discharge system *Phys. Rev. Lett.* **98**, 255001 DOI: 10.1103/PhysRevLett.98.255001

29 Slikboer E, Sobota A, Guaitella O, and Garcia-Caurel E 2018 Imaging axial and radial electric field components in dielectric targets under plasma exposure *J. Phys. D: Appl. Phys.* **51**, 115203 DOI: 10.1088/1361-6463/aaad99

30 Viegas P and Bourdon A 2020 Numerical study of jet-target interaction: influence of dielectric permittivity on the electric field experienced by the target *Plasma Chem. Plasma Process.* **40**, 661-683 DOI: 10.1007/s11090-019-10033-6

31 Pechereau F, Jansky J, and Bourdon A 2012 Simulation of the reignition of a discharge behind a dielectric layer in air at atmospheric pressure *Plasma Sources Sci. Technol.* **21**, 055011 DOI: 10.1088/0963-0252/21/5/055011

32 Opaits D F, Shneider M N, Miles R B, Likhanskii A V, and Macheret S O 2008 Surface charge

in dielectric barrier discharge plasma actuators *Phys. Plasmas* **15**, 073505 DOI: /10.1063/1.2955767

33 Slikboer E, Guaitella O, and Sobota A 2016 Time-resolved electric field measurements during and after the initialization of a kHz plasma jet - from streamers to guided streamers *Plasma Sources Sci. Technol.* **25**, 03LT04 DOI: 10.1088/0963-0252/25/3/03LT04

34 Kawasaki T, Arai Y, and Takada T 1991 Two-dimensional measurement of electrical surface charge distribution on insulating material by electrooptic pockels effect *Jpn. J. Appl. Phys.* **30**, 1262-1265 DOI: 10.1143/JJAP.30.1262

35 Wild R, Gerling T, Bussiahn R, Weltmann K D, and Stollenwerk L 2014 Phase-resolved measurement of electric charge deposited by an atmospheric pressure plasma jet on a dielectric surface *J. Phys. D: Appl. Phys.* **47**, 042001 DOI: 10.1088/0022-3727/47/4/042001

36 Ren C, Huang B, Zhang C, Qi B, Chen W, and Shao T 2023 Impact of surface charges on energy deposition in surface dielectric barrier discharge: a modeling investigation *Plasma Sources Sci. Technol.* **32**, 025004 DOI: 10.1088/1361-6595/acb4b9

37 Soloviev V R, Krivtsov V M, Shcherbanev S A, and Starikovskaia S M 2017 Evolution of nanosecond surface dielectric barrier discharge for negative polarity of a voltage pulse *Plasma Sources Sci. Technol.* **26**, 014001 DOI: 10.1088/0963-0252/26/1/014001

38 Sigmond R S 1984 The residual streamer channel: Return strokes and secondary streamers *J. Appl. Phys.* **56**, 1355 DOI: 10.1063/1.334126

39 Darny T, Pouvesle J-M, Puech V, Douat C, Dozias S, and Robert E 2017 Analysis of conductive target influence in plasma jet experiments through helium metastable and electric field measurements *Plasma Sources Sci. Technol.* **26**, 045008 DOI: 10.1088/1361-6595/aa5b15

40 Babaeva N Y and Naidis G V 2020 Reactive fluxes delivered by plasma jets to conductive dielectric surfaces during multiple reflections of ionization waves *J. Appl. Phys.* **128**, 203301 DOI: 10.1063/5.0019350

41 Mirzaee M, Simeni Simeni M, and Bruggeman P J 2020 Electric field dynamics in an atmospheric pressure helium plasma jet impinging on a substrate *Phys. Plasmas* **27**, 123505 DOI: 10.1063/5.0021837

42 Ono R and Komuro A 2020 Generation of the single-filament pulsed positive streamer discharge in atmospheric-pressure air and its comparison with two-dimensional simulation *J. Phys. D: Appl. Phys.* **53**, 035202 DOI: 10.1088/1361-6463/ab4e65

43 Ren C, Huang B, Qiu J, Zhang C, Qi B, Chen W, and Shao T 2022 Is an extended barrier-free discharge under nanosecond-pulse excitation really diffuse? *J. Phys. D: Appl. Phys.* **55**, 235204 DOI: 10.1088/1361-6463/ac4f0d

44 Zhu Y, Chen X, Wu Y, and Starikovskaia S M, PASSKEy code[software]. Available from http://www.plasma-tech.net/parser/passkey/ (Science and Technology of Plasma Dynamics Laboratory, Xi'an, China and Laboratoire de Physique des Plasmas, Paris, France, 2021).

45 Zhu Y, Chen X, Wu Y, Hao J, Ma X, Lu P, and Tardiveau P 2021 Simulation of ionization-wave discharges: a direct comparison between the fluid model and E-FISH measurements *Plasma Sources Sci. Technol.* **30**, 075025 DOI: 10.1088/1361-6595/ac0714

46 Malagon Romero A and Luque A 2018 A domain-decomposition method to implement electrostatic free boundary conditions in the radial direction for electric discharges *Comput. Phys. Commun.* **225**, 114-121 DOI: 10.1016/j.cpc.2018.01.003

47 Huang B, Zhang C, Zhu W, Lu X and Shao T 2021 Ionization waves in nanosecond pulsed atmospheric pressure plasma jets in argon *High Volt.* **6**, 655-73 DOI: 10.1049/hve.2.12067

48 Babaeva N Y, Tereshonok D V, and Naidis G V 2016 Fluid and hybrid modeling of nanosecond surface discharges: effect of polarity and secondary electrons emission *Plasma Sources Sci. Technol.* **25**, 044008 DOI: 10.1088/0963-0252/25/4/044008

49 Tholin F and Bourdon A 2013 Simulation of the hydrodynamic expansion following a nanosecond pulsed spark discharge in air at atmospheric pressure *J. Phys. D: Appl. Phys.* **46**, 365205 DOI: 10.1088/0022-3727/46/36/365205

50 COMSOL Multiphysics simulation package, version 6.0.

51 Kutasi K, Guerra V, and Sa P 2010 Theoretical insight into Ar-O2 surface-wave microwave discharges *J. Phys. D: Appl. Phys.* **43**, 175201 DOI: 10.1088/0022-3727/43/17/175201

52 Zhu Y, Lepikhin N D, Orel I S, Salmon A, Klochko A V, and Starikovskaia S M 2018 Optical actinometry of O-atoms in pulsed nanosecond capillary discharge: peculiarities of kinetics at high specific deposited energy *Plasma Sources Sci. Technol.* **27**, 075020 DOI: 10.1088/1361-6595/aac95f

53 Zhu Y and Starikovskaia S M 2018 Fast gas heating of nanosecond pulsed surface dielectric barrier discharge: spatial distribution and fractional contribution from kinetics *Plasma Sources Sci. Technol.* **27**, 124007 DOI: 10.1088/1361-6595/aaf40d

54 Saifutdinov A I 2022 Numerical study of various scenarios for the formation of atmospheric

pressure DC discharge characteristics in argon: from glow to arc discharge *Plasma Sources Sci. Technol.* **31**, 094008 DOI: 10.1088/1361-6595/ac89a7

55 Hagelaar G J M and Pitchford L C 2005 Solving the Boltzmann equation to obtain electron transport coefficients and rate coefficients for fluid models *Plasma Sources Sci. Technol.* **14**, 722-33 DOI: 10.1088/0963-0252/14/4/011

56 SIGLO database, Phelps database, TRINITI database (available at www.lxcat.net) (Accessed 13 March 2021)

57 Slikboer E, Guaitella O, Garcia-Caurel E, and Sobota A 2022 Towards plasma jet controlled charging of a dielectric target at grounded, biased, and floating potential *Sci. Rep.* **12**, 1157 DOI: 10.1038/s41598-022-05075-4

58 Norberg S A, Johnsen E, and Kushner M J 2015 Helium atmospheric pressure plasma jets touching dielectric and metal surfaces *J. Appl. Phys.* **118**, 013301 DOI: 10.1063/1.4923345

59 Zhang Q, Zhang L, Yang D, Schulze J, Wang Y and Bogaerts A 2020 Positive and negative streamer propagation in volume dielectric barrier discharges with planar and porous electrodes *Plasma Process Polym.* e2000234 DOI: 10.1002/ppap.202000234

60 Soloviev V R and Krivtsov V M 2009 Surface barrier discharge modeling for aerodynamic applications *J. Phys. D: Appl. Phys.* **42**, 125208 DOI: 10.1088/0022-3727/42/12/125208

61 Zhang Q, Nguyen-Smith R T, Beckfeld F, Liu Y, Mussenbrock T, Awakowicz P and Schulze J 2021 Computational study of simultaneous positive and negative streamer propagation in a twin surface dielectric barrier discharge via 2D PIC simulations *Plasma Sources Sci. Technol.* **30**, 075017 DOI: 10.1088/1361-6595/abf598

62 Ono R 2016 Optical diagnostics of reactive species in atmospheric-pressure nonthermal plasma *J. Phys. D: Appl. Phys.* **49**, 083001 DOI: 10.1088/0022-3727/49/8/083001

63 Bogaczyk M, Wild R, Stollenwerk L, and Wagner H E 2012 Surface charge accumulation and discharge development in diffuse and filamentary barrier discharges operating in He, N_2 and mixtures *J. Phys. D: Appl. Phys.* **45**, 465202 DOI: 10.1088/0022-3727/45/46/465202

64 Herrmann A, Margot J, and Hamdan A 2024 Experimental and 2D fluid simulation of a streamer discharge in air over a water surface *Plasma Sources Sci. Technol.* **33**, 025022 DOI: 10.1088/1361-6595/ad286f

65 Hagelaar G J M, de Hoog F J, and Kroesen G M W 2000 Boundary conditions in fluid models of

gas discharges *Phys. Rev. E* **62**, 1452-1454 DOI: 10.1103/PhysRevE.62.1452

66 Pechereau F, Jansky J, and Bourdon A 2012 Simulation of the reignition of a discharge behind a dielectric layer in air at atmospheric pressure *Plasma Sources Sci. Technol.* **21**, 055011 DOI: 10.1088/0963-0252/21/5/055011

67 Nagaraja S, Yang V, and Adamovish I 2013 Multi-scale modelling of pulsed nanosecond dielectric barrier plasma discharges in plane-to-plane geometry *J. Phys. D: Appl. Phys.* **46**, 155205 DOI: 10.1088/0022-3727/46/15/155205

68 Vitello P A, Penetrante B M, and Bardsley J N 1994 Simulation of negative-streamer dynamics in nitrogen *Phys. Rev. E* **49**, 5574-5598 DOI: 10.1103/PhysRevE.49.5574

69 Segur P, Bourdon A, Marode E, Bessieres D, and Paillol J H 2006 The use of an improved Eddington approximation to facilitate the calculation of photoionization in streamer discharges *Plasma Sources Sci. Technol.* **15**, 648-660 DOI: 10.1088/0963-0252/15/4/009

70 Bourdon A, Pasko V P, Liu N Y, Celestin S, Segur P, and Marode E 2007 Efficient models for photoionization produced by non-thermal gas discharges in air based on radiative transfer and the Helmholtz equations *Plasma Sources Sci. Technol.* **16**, 656-678 DOI: 10.1088/0963-0252/16/3/026

71 Pancheshnyi Sergey 2015 Photoionization produced by low-current discharges in O_2, air, N_2 and CO_2 *Plasma Sources Sci. Technol.* **24**, 015023 DOI: 10.1088/0963-0252/24/1/015023

72 Kramida A, Ralchenko Y, Reader J and NIST ASD Team (2023). *NIST Atomic Spectra Database* (version 5.11), [Online]. Available: https://physics.nist.gov/asd [Fri Jan 26 2024]. National Institute of Standards and Technology, Gaithersburg, MD. DOI: 10.18434/T4W30F

73 Fennelly J A and Torr D G 1992 Photoionization and photoabsorption cross sections of O, N_2, O_2, and N for aeronomic calculations *Atom. Data Nucl. Data* **51**, 321 DOI: 10.1016/0092-640X(92)90004-2

74 Cernak M, Hoder T, and Bonaventura Z 2020 Streamer breakdown: cathode spot formation, Trichel pulses and cathode-sheath instabilities *Plasma Sources Sci. Technol.* **29**, 013001 DOI: 10.1088/1361-6595/ab5051